

**ARTICLE TYPE**

# A fast and accurate method for transport and dispersion of phosphogypsum in coastal zones: Application to Jorf Lasfar

Abdelouahed Ouardghi<sup>1</sup> | Mohammed Seaid<sup>2</sup> | Mofdi El-Amrani\*<sup>3</sup> | Nabil El Mocayd<sup>1,4</sup>

<sup>1</sup>International Water Research Institute,  
University Mohammed VI Polytechnic,  
Benguerir, Morocco

<sup>2</sup>Department of Engineering, University of  
Durham, South Road, Durham DH1 3LE,  
UK

<sup>3</sup>Dpto. Matemáticas Aplicada, Universidad  
Rey Juan Carlos, 28933 Móstoles-Madrid,  
Spain

<sup>4</sup>Institute of Applied Physics, University  
Mohammed VI Polytechnic, Benguerir,  
Morocco

**Correspondence**

\*Mofdi El-Amrani Email:  
mofdi.elamrani@urjc.es

**Summary**

We present a numerical method for modelling and simulation of transport and dispersion of phosphogypsum in the Jorf Lasfar coastal zone located on the Atlantic Ocean at Morocco. The governing equations consist of the well-established barotropic ocean model including the barometric pressure, friction terms, Coriolis and wind stresses. To model transport and dispersion of phosphogypsum we consider an advection-diffusion equation with an anisotropic dispersion tensor and source terms. As a numerical solver, we propose a novel multilevel adaptive semi-Lagrangian finite element method. The proposed method combines the modified method of characteristics to deal with convection terms, the finite element discretization to handle complex geometries, a projection-based algorithm to solve the Stokes problem, and an adaptive  $L^2$ -projection using quadrature rules to improve the efficiency and accuracy of the method. Numerical results are presented to demonstrate the high resolution of the proposed method and to confirm its capability to provide accurate and efficient simulations for transport and dispersion of phosphogypsum in the Jorf Lasfar coastal zone.

**KEYWORDS:**

Jorf Lasfar coastal zone, Incompressible Navier-Stokes equations, Enriched finite elements, semi-Lagrangian method,  $L^2$  projection, Adaptive algorithm.

## 1 | INTRODUCTION

Jorf Lasfar hosts one of the largest industrial plants for phosphate transformation being Africa's largest mineral port and it is a deep-sea port with a diverse, energy-intensive mineral function. It is a commercial port and a hub for phosphate, fertilizers, and other chemicals. Jorf Lasfar is located 17 km from the city of El Jadida and 120 km from Casablanca, it enjoys great connectivity and a back-country rich in diverse resources, see Figure 1. In addition to the OCP plants, Jorf Lasfar accommodates a thermal power plant and hydrocarbon storage units. The main industrial objective is to transform the phosphate rock into phosphate-based fertilizers, phosphoric acid or other phosphate derivatives. Through this production process, a considerable amount of a by-product called phosphoGypsum (PG) is generated, see<sup>1</sup>. According to<sup>2</sup>, for every ton of produced phosphoric acid, five tons of the PG are generated. For this reason, despite the tremendous efforts undertaken to reuse the PG in agriculture, in the cement

industry, and road building, the huge amount of PG produced cannot be totally injected into the aforementioned industries. Therefore, managers have decided to release their waste in the high seas<sup>3</sup>, which has various non-negligible environmental and ecological impacts, especially on the touristic areas near the industrial plant. The release of PG at the Jorf Lasfar site affects a large distance along the coastline and beaches, especially in the region of Doukkala at the middle of Morocco. This includes the touristic zone of El Jadida, which is considered one of the busiest beaches during the summer. Furthermore, other sea-related activities happening in this particular area including fishing are severely harmed by the release of PG. While a major part of past studies were dedicated to assess the risk of PG on the fauna and the flora in the neighborhood<sup>4,5,1</sup>, to the best of our knowledge, few attention was given to the impact of the oceanic circulation on the transport and the dispersion of PG in the high seas and near coastlines. According to a new initiative of the United Nations called the Ocean Decade, much effort should be made in order to enhance sustainability for the oceans<sup>6</sup>. Monitoring activities such as PG release are therefore of the utmost importance within this framework. Based on the study reported in<sup>7</sup>, modeling of ocean dynamics in order to monitor and predict the ocean state and its impact on waste dispersion such as PG is an important ingredient within this context. The present work aims at addressing this particular issue for the case of PG release at Jorf Lasfar and also modeling pollution transport in the ocean is very challenging for different reasons. In fact, oceanic circulation encompasses several complex physical mechanisms happening at different time and space scales that are hardly modelled with the same level of accuracy, see<sup>8,9,10</sup> among others. Developing accurate numerical tools to predict the state of the ocean is therefore still at the state-of-art, see<sup>11</sup>.

In general, an ocean model solves the incompressible Navier-Stokes equations equipped with a class of oceanic source terms<sup>12</sup>, whereas the dispersion of pollutants is described using an advection-diffusion equation, see for example<sup>13</sup>. Finite element methods have largely been used as the main numerical method in order to solve these equations, compare<sup>14</sup> among others. When using finite element methods, one can distinguish between two general methods namely Eulerian and Lagrangian techniques. Both methods have been extensively used for numerical simulations of complex flows. However, the Eulerian-base finite element methods fail to achieve good accuracy when dealing with some specific flow conditions such as sharp fronts, shocks, vortex shedding, and boundary layers. Furthermore, because of the stability conditions, this class of methods struggles with convection-dominated problems such as oceanic flows. On the other hand, Galerkin-characteristics finite element methods allow to overcome the previously stated difficulties within a good accuracy, see for instance<sup>14</sup>. In the current work, the governing equations consist of the well-established barotropic ocean model including bathymetric forces, Coriolis effects, friction terms, eddy-diffusion, and wind stresses. To model the transport and dispersion of phosphogypsum, an advection-diffusion equation involving an anisotropic dispersion tensor and a source term is considered. The coupled flow and transport model yields a system with the property that the convective terms are distinctly more dominant than the diffusive terms, especially when certain nondimensional parameters exceed some threshold values. As examples of these parameters, we mention the Peclet number for advection-diffusion equations and the Reynolds number for the incompressible Navier-Stokes equations. At high values of these numbers, the convective term is known to be a source of computational difficulties and nonphysical oscillations. The goal of this research is to develop a stable, reliable, and accurate numerical method capable of producing accurate solutions to the coupled flow and transport system in the Jorf Lasfar coastlines. It should be stressed that it is difficult to validate numerical results for the transport and dispersion of phosphogypsum against measurements from field experiments. The main difficulties lie essentially in the empirical formulas needed to close the transport and dispersion of the phosphogypsum model and also in the calibration of the parameters involved in the flow modelling. Therefore, the solutions are first assessed over some benchmark examples and then, simulations are compared qualitatively against remote sensing observation data. It should be stressed that semi-Lagrangian methods for fluids have been widely used in the area of computational fluid dynamics. The basic concept behind these semi-Lagrangian finite element techniques is to reformulate the governing equations using the Lagrangian coordinates defined by the characteristic curves associated with the problem under consideration. Indeed, semi-Lagrangian approaches combine the advection term and time derivative into a directional derivative along the characteristic curves, which is considered a characteristic time-stepping method. Thus, the advantage of the semi-Lagrangian schemes is the property that they are CFL-condition free. This fact means that we can exceed time steps imposed by the CFL stability requirement in Eulerian-based methods, which results in a significant reduction in time truncation errors and saves execution time.

The main objective of the current study lies in investigating a multilevel adaptive enriched semi-Lagrangian finite element method for the numerical simulation of transport and dispersion of phosphogypsum in the Jorf Lasfar port. This class of methods has been proposed for the first time in<sup>15,16</sup> where an  $L^2$ -projection semi-Lagrangian finite element approach has been introduced for solving convection-diffusion and incompressible Navier-Stokes problems. In this approach, the convective terms which are usually known as a source of computational difficulties are dealt with using the semi-Lagrangian method whereas, the diffusive terms are handled using a mixed finite element method. However, when dealing with real applications, solving

convection-dominated flow problems using this class of methods becomes computationally expensive due to the huge density of quadratures needed by the  $L^2$ -projection for the computation of solutions at the departure points. To overcome this drawback, a novel class of adaptive enriched semi-Lagrangian finite element method has been proposed for convection-diffusion problems in<sup>17</sup>, for incompressible Navier-Stokes equations in<sup>18</sup> and for coupled Navier-Stokes/Boussinesq equations in<sup>19</sup>. This approach enriches locally the approximation of integrals in the  $L^2$ -projection using a family of quadrature rules which allows for spatial discretization on coarse fixed meshes. Moreover, the enrichment points are adjusted as needed without refining the mesh throughout the time integration process and therefore, the associated linear systems preserve the same size and structure during the simulation. In practice, a semi-Lagrangian method tracks backwards the numerical solution at a time level in the departure points of a discrete set of virtual (backward) Lagrangian particles that arrive at a regular set of gridpoints at the next time level. To evaluate the departure points, a second-order extrapolation based on the midpoint rule is used in previous works<sup>18,17,19</sup>. However, these typical solvers are inappropriate to compute departure points because of the feature of the quick expansion of the invariants in large-time computations<sup>20</sup>. Consequently, the overall accuracy of the semi-Lagrangian schemes is highly sensitive to the evaluation of the departure points. In this work, we adopt the symplectic integrators presented in<sup>21</sup> which are based on the Hamilton variational principle to evaluate the departure points. These methods are considered as structure-preserving methods and they have the potential to deal with the rapid growth of Hamiltonian even in long-time simulations and can guarantee a correct streamline tracking. Another advantage of the proposed approach over those presented in<sup>18,17,19</sup> lies in the efficiency of the search-locate algorithm used for identifying the mesh elements where departure points lie in the computational domain. Indeed, the search-locate algorithm is improved to efficiently deal with the high number of points that need to be located in a discretized domain. Furthermore, in our previous works<sup>18,19</sup> a direct gradient conjugate solver has been used for solving the stokes equations. However, the main drawback of this method is the computational cost especially when solving the large systems of algebraic equations associated with the discretized problem. To overcome this drawback, we proposed in the current work a coupled projection scheme based on a rotational pressure correction with a second-order backward difference formula for the time integration presented in<sup>22</sup>. Compared to the standard projection methods, the presence of the previous gradient step in the velocity prediction problem improves the accuracy order of the method. Moreover, the rotational pressure correction projection enhances the method to avoid artificial boundary conditions on the pressure and improves the rate of convergence of the pressure. It should also be noted that the proposed adaptive enriched semi-Lagrangian finite element method uses the well-established gradient-based error indicators to identify areas that need to be enriched in the computational domain. Multiple quadratures are used for enrichments in the  $L^2$ -projection, which allows for considerable efficiency because the computational mesh is kept fixed and re-utilized throughout the simulation process, as opposed to  $h$ -adaptive finite element approaches with gradient-based error indicators, see for example,<sup>23,24,25,26,27,28,29</sup>. Indeed,  $h$ -adaptive techniques with gradient-based error indicators require an initial coarse mesh to evaluate a primary solution for the error estimation. Because of the coarse mesh used in the approximation, this causes error accumulation and the computation cost becomes prohibitive due to the many interpolations between adaptive meshes. Several numerical examples for transport and dispersion problems are used to test the performance of the proposed approaches. The enriched semi-Lagrangian finite element method is examined for various levels of enrichment and mesh refinements. The obtained results are also compared to those obtained using the conventional methods.

This paper is organized as follows. In Section 2 we present the governing equations and their finite element discretization. The proposed numerical method is presented in Section 3. This section includes symplectic semi-Lagrangian scheme, local enrichment and projection method for solving the Stokes problem. Section 4 is devoted to the development of the adaptive enriched semi-Lagrangian finite element method. The criteria used for the adaptation process is also discussed in this section. In Section 5, we examine the numerical performance of the proposed method using two examples of dispersion problems including transport and dispersion of phosphogypsum in the port of Jorf Lasfar. Concluding remarks are summarized in Section 6.

## 2 | MATHEMATICAL MODELS

Several models exist in the literature to describe the hydrodynamics and water flows in rivers and oceans, see for instance<sup>30,31</sup>. In the situations where the pressure can be assumed hydrostatic and the bathymetric forces may become strong, the well-established shallow water equations are most suitable for their modelling. However, in oceanography and problems as those considered in this work, these forces are very weak and the pressure still persists within the flows and therefore the barotropic model is considered to be the most appropriate for these situations. For a detailed comparison between shallow water and barotropic



**Figure 1** Map illustrating the location of Jorf Lasfar.

model, we refer to<sup>32</sup> and further discussions are therein. In the present study, we consider a barotropic ocean model for the flow along with a convection-diffusion equation for the concentration transport as

$$\begin{aligned} \nabla \cdot \mathbf{U} &= 0, \\ \frac{\partial \mathbf{U}}{\partial t} + \mathbf{U} \cdot \nabla \mathbf{U} + \nabla p - \nu \Delta \mathbf{U} &= f \mathbf{U}^\perp - \gamma \mathbf{U} + \frac{\boldsymbol{\tau}}{H} + \beta (C - C_\infty) \mathbf{e}, \\ \frac{\partial C}{\partial t} + \mathbf{U} \cdot \nabla C - \nabla \cdot (\mathbf{D} \nabla C) &= S, \end{aligned} \quad (1)$$

where  $\Omega \subset \mathbb{R}^2$  is a bounded domain with boundary  $\Gamma$ ,  $\mathbf{U} = (U, V)^\top$  the depth-averaged horizontal velocity field defined by

$$\mathbf{U}(t, \mathbf{x}) = \frac{1}{H} \int_{-H}^0 \mathbf{u}(t, x, y, z) dz,$$

with  $\mathbf{u}$  is the velocity field,  $H$  the depth of the water measured from the undisturbed water surface. In (1),  $p$  denotes the pressure,  $f$  the Coriolis parameter,  $\gamma$  to the bottom friction coefficient,  $\nu$  the kinematic viscosity,  $\boldsymbol{\tau}$  the wind stress acting on the upper surface,  $\beta$  the coefficient of solute expansion,  $C$  the pollutant concentration,  $S(t, \mathbf{x})$  the source term,  $C_\infty$  the reference concentration and  $\mathbf{U}^\perp = (V, -U)^\top$ . It should be stressed that the flow equations (1) account for the barometric pressure, Coriolis effects, friction terms, eddy-diffusion, and wind stresses. In this class of applications, the influence of the bathymetry in the barotropic ocean model appears in conjunction with the wind stress acting on the upper surface such that large effects are expected for shallow waters and strong winds<sup>30,31</sup>. Notice that at deep waters or weak winds, the influence of the bathymetry on the model is minimal and it can be neglected. Unlike the conventional shallow water equations for which effects of the bathymetry appear as source terms involving its gradient, the barotropic ocean model (1) assumes that the bathymetric variation is very small and therefore cancels out in the governing equations but it still appears within the wind stresses, see for example<sup>32</sup>.

In (1),  $\mathbf{D}$  is the diffusion tensor defined as

$$\mathbf{D} = \begin{pmatrix} D_{11} & D_{12} \\ D_{21} & D_{22} \end{pmatrix}, \quad (2)$$

where the coefficients  $D_{11}$ ,  $D_{12}$ ,  $D_{21}$  and  $D_{22}$  are defined by the Fickian dispersion tensor as

$$\begin{aligned} D_{11} &= D_m + \frac{\alpha_L U^2 + \alpha_T V^2}{\sqrt{U^2 + V^2}}, \\ D_{12} &= D_{21} = (\alpha_L - \alpha_T) \frac{UV}{\sqrt{U^2 + V^2}}, \\ D_{22} &= D_m + \frac{\alpha_L V^2 + \alpha_T U^2}{\sqrt{U^2 + V^2}}, \end{aligned} \quad (3)$$

where  $D_m$  is the molecular dispersion coefficient,  $\alpha_L$  and  $\alpha_T$  are the longitudinal and transverse dispersion coefficients, respectively. Note that in general, the coriolis force mainly occurs in three-dimensional models used in the ocean recirculation. However, since the model considered in the present work is obtained by depth-averaging the three-dimensional equations, these terms are inherited from the full model and they should be accounted for in large water areas such as the one used in our study. Obviously, the impact of these terms on the flow recirculation would depend on the magnitude of the velocity field and the Coriolis parameter  $f$  which varies with the rotation of the earth<sup>30,31</sup>. It should be noted that equations (1) are equipped with appropriate boundary and initial conditions to produce a well-posed mathematical problem.

For solving the equations (1)-(3), the simulation domain  $\bar{\Omega} = \Omega \cup \Gamma$  is discretized into a quasi-uniform partition  $\Omega_h \subset \Omega$  of triangular elements  $\mathcal{T}_k$  such that  $\bar{\Omega} = \cup_{k=1}^{N_e} \mathcal{T}_k$ , where  $N_e$  is the number of elements of  $\Omega_h$  and  $h$  is a space discretization parameter. For the conforming finite element spaces for the velocity/concentration and pressure, we use the mixed Taylor-Hood finite elements  $P_2$ - $P_1$  *i.e.*, quadratic elements for the velocity/concentration and linear elements for the pressure. It is well-known that for the mixed finite element formulation, the discrete velocity and pressure fields satisfy the inf-sup condition, see for instance<sup>16</sup>. The finite element spaces associated to the mixed formulation are defined as

$$V_h = \left\{ U_h \in C^0(\Omega) : U_h|_{\mathcal{T}_k} \in P_2(\mathcal{T}_k), \forall \mathcal{T}_k \in \Omega_h \right\}, \quad P_h = \left\{ p_h \in C^0(\Omega) : p_h|_{\mathcal{T}_k} \in P_1(\mathcal{T}_k), \forall \mathcal{T}_k \in \Omega_h \right\},$$

where  $P_1(\mathcal{T}_k)$  and  $P_2(\mathcal{T}_k)$  are polynomial spaces of degree 1 and 2, respectively, defined in the element  $\mathcal{T}_k$ . Since the velocity field is a vector of two components, the associated finite element space is defined as  $\mathbf{V}_h = V_h \times V_h$ . For the time discretization, the time interval  $[0, T]$  is also divided into sub-intervals  $[t_n, t_{n+1}]$  of a fixed length  $\Delta t = t_{n+1} - t_n$  for  $n \geq 0$ . In the following, we adopt the notation  $w_h^n := w(\mathbf{x}_h, t_n)$  to denote the value of a function  $w$  at time  $t_n$  in the position  $\mathbf{x}_h$ . Hence, the approximate values  $\mathbf{U}_h^n(\mathbf{x}) \in \mathbf{V}_h$ ,  $p_h^n(\mathbf{x}) \in P_h$  and  $C_h^n(\mathbf{x}) \in V_h$  are formulated as

$$\mathbf{U}_h^n(\mathbf{x}) = \sum_{j=1}^{M_v} \mathbf{U}_j^n \phi_j(\mathbf{x}), \quad p_h^n(\mathbf{x}) = \sum_{l=1}^{M_p} P_l^n \psi_l(\mathbf{x}), \quad C_h^n(\mathbf{x}) = \sum_{j=1}^{M_v} C_j^n \phi_j(\mathbf{x}), \quad (4)$$

where  $M_v$  and  $M_p$  are respectively, the number degrees of freedom associated with velocity/concentration and pressure in  $\Omega_h$ . The solutions  $\mathbf{U}_j^n = \left( U_j^n, V_j^n \right)^\top$ ,  $P_l^n$  and  $C_j^n$  are the corresponding nodal values of  $\mathbf{U}_h^n(\mathbf{x})$ ,  $p_h^n(\mathbf{x})$  and  $C_h^n(\mathbf{x})$ , respectively. These values are evaluated as  $\mathbf{U}_j^n = \mathbf{U}_h^n(\mathbf{x}_j)$ ,  $P_l^n = p_h^n(\mathbf{y}_l)$  and  $C_j^n = C_h^n(\mathbf{x}_j)$ , respectively, where  $\{\mathbf{y}_l\}_{l=1}^{M_p}$  is the set of mesh points in  $\Omega_h$  and  $\{\mathbf{x}_j\}_{j=1}^{M_v}$  is the set containing the mesh nodes in addition to the mid-edge nodes. Here,  $M_p < M_v$ ,  $\{\mathbf{y}_l\}_l \subset \{\mathbf{x}_j\}_j$  and  $\{\phi_j\}_{j=1}^{M_v}$  and  $\{\psi_l\}_{l=1}^{M_p}$  are respectively, the set of global nodal basis functions of the velocity and the pressure spaces, characterized by the property  $\phi_i(\mathbf{x}_j) = \delta_{ij}$  and  $\psi_i(\mathbf{y}_l) = \delta_{il}$  with  $\delta$  denoting the Kronecker symbol.

### 3 | NUMERICAL METHODS

The semi-Lagrangian finite element method belongs to fractional-step techniques where the convective parts in (1) are decoupled from the Stokes part in the time integration procedure. Let  $\mathbf{U}_h \in \mathbf{V}_h$ ,  $C_h \in V_h$  and  $p_h \in P_h$  be the discrete velocity, temperature and pressure, respectively. Thus, at each time step the solutions are updated by first solving the convection equations using the

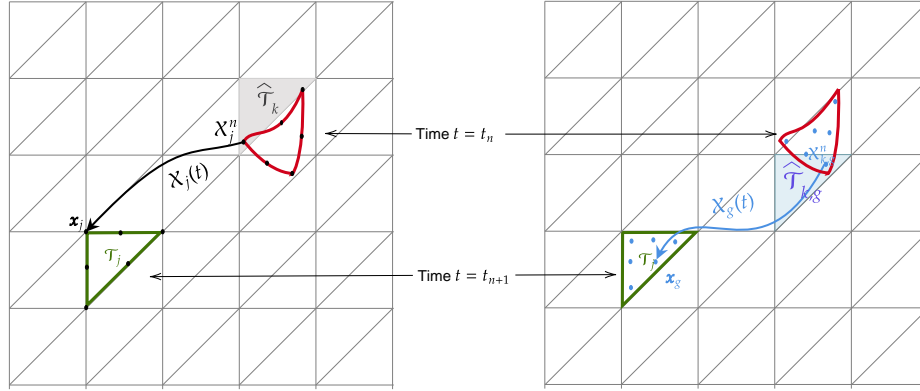


**Figure 2** An illustration displaying the key parameters utilized for approaching the departure points in the conventional method (black line) and the  $L^2$ -projection method (blue line).

semi-Lagrangian approach

$$\begin{aligned}\frac{D\mathbf{U}_h}{Dt} &:= \frac{\partial \mathbf{U}_h}{\partial t} + \mathbf{U}_h \cdot \nabla \mathbf{U}_h = \mathbf{0}, \\ \frac{DC_h}{Dt} &:= \frac{\partial C_h}{\partial t} + \mathbf{U}_h \cdot \nabla C_h = 0,\end{aligned}\quad (5)$$

followed by the generalized Stokes equations

$$\begin{aligned}\nabla \cdot \mathbf{U}_h &= 0, \\ \frac{D\mathbf{U}_h}{Dt} + \nabla p_h - \nu \Delta \mathbf{U}_h &= f \mathbf{U}_h^\perp - \gamma \mathbf{U}_h + \frac{\tau}{H} + \beta (C_h - C_\infty) \mathbf{e}, \\ \frac{DC_h}{Dt} - \nabla \cdot (\mathbf{D} \nabla C_h) &= S.\end{aligned}\quad (6)$$

In (5),  $\frac{D}{Dt} =: \frac{\partial}{\partial t} + \mathbf{U}_h \cdot \nabla$  is the material (total) derivative associated with flow velocity  $\mathbf{U}_h$ . In the subsequent section, we focus on the solution of the convection equations (5) using a symplectic semi-Lagrangian method. In the semi-Lagrangian method, the value of the transported fields in equations (5) are constant along the trajectory of a fluid particle that travels from a departure point at time  $t_n$  and arrives to the gridpoint  $\mathbf{x}_j$  at time  $t_{n+1}$ . This gridpoint is referred to as the arrival point and the particle trajectory is referred to as the characteristic curve. Accordingly, the value that we require at the arrival point is equal to the value of the field at the departure point. The travel of a fluid particle is associated with the velocity field  $\mathbf{U}_h$  along a characteristic curve  $\chi_j(t)$ , which fulfills the following first-order ordinary differential equation

$$\begin{aligned}\frac{d\chi_j(t)}{dt} &= \mathbf{U}_h(\chi_j(t), t), \quad t \in [t_n, t_{n+1}], \\ \chi_j(t_{n+1}) &= \mathbf{x}_j.\end{aligned}\quad (7)$$

Therefore,  $\chi_j(t_n) = (X_j(t_n), Y_j(t_n))^\top$  is the departure point at time  $t_n$  of the particle that will attain the point  $\mathbf{x}_j = (x_j, y_j)^\top$  at time  $t_{n+1}$  as illustrated in Figure 2. For simplicity purposes, we note by  $\chi_j^n$  the departure point  $\chi_j(t_n)$ .

### 3.1 | Calculation of departure points

The practical use of the conventional semi-Lagrangian method requires in a first step an approximation of the solution of (7). This solution can be formulated as

$$\chi_j^n = \mathbf{x}_j - \int_{t_n}^{t_{n+1}} \mathbf{U}_h(\chi_j(t), t) dt.\quad (8)$$

In the Lagrangian framework, the equation (7) is usually evaluated using numerical integration techniques such as the Runge-Kutta and Euler approaches<sup>18,17,19,15,16</sup>. However, while these solvers are generic, they have the inconvenient feature of quick system energy development (Hamiltonian) in long-time computations and they are inappropriate for particle tracking since they are not structure-preserving (SP) methods, see for example<sup>20</sup>. It has been shown in<sup>21</sup> that when non-geometric integrators are employed, such as the widely used Runge-Kutta approaches, the obtained results are less accurate and more diffuse. Indeed, the so-called symplectic integrators have the potential to deal with the rapid growth of Hamiltonian even in long-time simulations and can guarantee a correct streamline tracking. Since the symplectic integrators are only appropriate for Hamiltonian systems, a stream function  $\psi$  can be used to express equation (7) for the incompressible flow. Thus, the characteristics trajectory  $\chi = (X, Y)^\top$  can be reformulated as

$$\begin{aligned}\frac{dX}{dt} &= \frac{d\psi}{dY}, \\ \frac{dY}{dt} &= -\frac{d\psi}{dX},\end{aligned}\quad (9)$$

where the stream-function  $\psi$  is considered as the Hamiltonian and the pair  $(X, Y)^\top$  is considered as the canonical pair. Consequently, the equations (9) are a Hamiltonian system for which it is possible to use symplectic integrators to evaluate integration in (8). In the present study, we consider the one-step method presented in<sup>21</sup> to evaluate the solution of (7) as

$$\chi_{r+1} = \Phi_{\Delta t}(\chi_r), \quad (10)$$

where the method  $\Phi_{\Delta t}$  is assumed to be a second-order method and time symmetric *i.e.*,  $\Phi_{\Delta t} \circ \Phi_{-\Delta t} = \mathbf{I}$ , with  $\circ$  and  $\mathbf{I}$  represent the function compositions symbol and the identity operator, respectively. For example, these requirements are satisfied by the implicit midpoint scheme and the Verlet method. An example of composite symplectic method is the *Yoshida* technique given by

$$\chi_{r+1} = \Phi_{\alpha\Delta t} \circ \Phi_{(1-2\alpha)\Delta t} \circ \Phi_{\alpha\Delta t}(\chi_r), \quad (11)$$

where  $\alpha = \frac{1}{3} \left( 2 + 2^{\frac{1}{3}} + 2^{-\frac{1}{3}} \right)$  is chosen to guarantee a fourth-order accuracy, see example<sup>4</sup>. In what follows, we choose  $\Phi_{\Delta t}$  to be the following implicit midpoint scheme

$$\chi_{r+1} = \chi_r - \Delta t \mathbf{U}_h \left( \frac{1}{2} (\chi_r + \chi_{r+1}), \frac{\Delta t}{2} \right), \quad (12)$$

which can be solved using Newton's method. The solution of the symplectic integrator is the departure point  $\chi_j^n$  at time  $t_n$  of the trajectory of a particle located at the gridpoint  $\mathbf{x}_j$  at time  $t_{n+1}$ . In terms of the particle movement, the transported quantities  $\mathbf{U}$  and  $\mathbf{C}$  in (5) are invariant along characteristic curves of the flow and are automatically transported by the particle's motion. Therefore, the semi-Lagrangian solution of (5) can be expressed as

$$\mathbf{U}_h^{n+1}(\mathbf{x}_j) = \mathbf{U}_h^n(\chi_j^n), \quad \mathbf{C}_h^{n+1}(\mathbf{x}_j) = \mathbf{C}_h^n(\chi_j^n). \quad (13)$$

However, the approximated departure point  $\chi_j^n$  does not necessarily coincide with a gridpoint in  $\Omega_h$ . As a result, a search-locate algorithm is required to find the element  $\hat{\mathcal{T}}_j$  where  $\chi_j^n$  belongs. In the current work, we use the method developed in<sup>33,34</sup>. Hence, to determine the host element  $\hat{\mathcal{T}}_j$  of the departure point  $\chi_j^n$ , we chose an initial guess  $\mathcal{T}_s$ , then we check if the departure point belongs to this element, else, we select one of its neighbor elements according to a selection criterion, then we repeat the process. In order to do so, we consider the on-to-one mapping  $\mathcal{F}_s$  from a reference element  $\mathcal{T}^*$  to the element  $\mathcal{T}_s$ , where the reference element  $\mathcal{T}^*$  for triangular mesh is defined as

$$\mathcal{T}^* = \left\{ (p, q) : 0 \leq p, q \leq 1, \quad 0 \leq 1 - p - q \leq 1 \right\}, \quad (14)$$

or

$$\mathcal{T}^* = \left\{ (p, q) : \min_i(\mathcal{N}_i(p, q)) \geq 0 \quad \text{and} \quad \max_i(\mathcal{N}_i(p, q)) \leq 1 \right\}, \quad (15)$$

where  $\mathcal{N}_i$ ,  $i = 1, \dots, N$  are the shape functions defined on the reference element  $\mathcal{T}^*$ . Therefore, for any  $\mathbf{x}_p = (x_p, y_p)^\top \in \mathcal{T}_s$ , there exists a point  $\mathbf{p}^* = (p^*, q^*) \in \mathcal{T}^*$  such that

$$\mathbf{x}_p - \mathbf{F}_s(\mathbf{p}^*) = \mathbf{0}. \quad (16)$$

Thus, if there is  $\mathbf{p}^*$  in  $\mathcal{T}^*$  satisfying (16), then  $\mathbf{x}_p$  belongs to the element  $\mathcal{T}_s$ . Hence, we search for a solution  $\mathbf{p}^*$  of (16) in  $\mathcal{T}^*$  using Newton method as follows:

Let  $\mathbf{x}_p \in \mathcal{T}_s$  and  $\mathbf{p}^0 = (p^0, q^0)^\top \in \mathcal{T}^*$ , then for  $k \geq 0$

$$\mathbf{p}^{k+1} = \mathbf{p}^k - \mathbf{J}_{\mathcal{F}_s}^{-1}(\mathbf{x}_p - \mathcal{F}_s(\mathbf{p}^k)), \quad (17)$$

**Algorithm 1** Search-locate algorithm

- 
- 1: Given  $\chi_j$
  - 2: Chose an arbitrary point  $\mathbf{p}^0 = (p^0, q^0)^\top$  in the reference element  $\mathcal{T}^*$
  - 3: Select an initial guess for the host element  $\mathcal{T}_s$
  - 4: Construct the mapping  $\mathcal{F}_s$  from  $\mathcal{T}^*$  to  $\mathcal{T}_s$
  - 5: Compute  $\mathbf{p}^* = (p^*, q^*)^\top$  the solution of equation (17)
  - 6: **if**  $\mathbf{p}^*$  in  $\mathcal{T}^*$  **then**
  - 7: The host element  $\hat{\mathcal{T}}_j$  of  $\chi_j$  is  $\mathcal{T}_s$ . (i.e.  $\hat{\mathcal{T}}_j \equiv \mathcal{T}_s$ )
  - 8: Stop
  - 9: **else**
  - 10: Apply the selection criteria to select a neighboring element
  - 11: Go to step 4
  - 12: **end if**
- 

where  $\mathbf{J}_{\mathcal{F}_s}^{-1}$  is the inverse of the Jacobian matrix  $\mathbf{J}_{\mathcal{F}_s}$  of the mapping  $\mathcal{F}_s$ . If  $\mathbf{x}_p \in \mathcal{T}_s$ , the Newton method (17) will converge to the unique solution  $\mathbf{p}^* \in \mathcal{T}^*$  independently of the initial guess  $\mathbf{p}^0 \in \mathcal{T}^*$ . Since  $\mathcal{T}_s$  is an arbitrary element, then we must test whether  $\mathbf{p}^{k+1}$  is in  $\mathcal{T}^*$  or not. Thus, using (15) we have  $\mathbf{p}^{k+1} \in \mathcal{T}^*$  if

$$\min_i(\mathcal{N}_i(\mathbf{p}^{k+1})) \geq 0 \quad \text{and} \quad \max_i(\mathcal{N}_i(\mathbf{p}^{k+1})) \leq 1.$$

If the iterate  $\mathbf{p}^{k+1} \notin \mathcal{T}^*$ , then  $\mathbf{x}_p \notin \mathcal{T}_s$ , because that, there is no  $\mathbf{p}^* \in \mathcal{T}^*$  such that (16) holds. Thus, a neighboring element of  $\mathcal{T}_s$  must be selected and reconsider the equation (17) for the new guess. The selection criteria used in this work can be expressed as:

- Let  $l = \text{index}(\min_i(\mathcal{N}_i(\mathbf{p}^{k+1})))$
- Select the element  $\mathcal{T}_r$  such that  $\Gamma_{sr} = \mathcal{T}_s \cap \mathcal{T}_r$  is the side of  $\mathcal{T}_s$  opposite to the vertex  $\mathbf{x}_l$ .

In summary, the search-locate algorithm for departure points carried out using Algorithm 1.

Once the departure point  $\chi_j^n$  and its host element  $\hat{\mathcal{T}}_j$  are determined, the solutions in departure point at time  $t_n$  can be interpolated from the known values at the vertices of  $\hat{\mathcal{T}}_j$  as

$$\mathbf{U}_h^n(\chi_j^n) = \sum_{i=1}^N \mathbf{U}_h^n(\hat{\mathbf{x}}_i) \varphi_i(\chi_j^n), \quad C_h^n(\chi_j^n) = \sum_{i=1}^N C_h^n(\hat{\mathbf{x}}_i) \varphi_i(\chi_j^n), \quad (18)$$

where  $\{\varphi_i\}_{i=1}^N$  are the local shape functions of the element  $\hat{\mathcal{T}}_j$ ,  $N$  is the number of nodes which define the velocity/concentration mesh type, and  $\{\hat{\mathbf{x}}_i\}_{i=1}^N$  are the vertices of the element  $\hat{\mathcal{T}}_j$ . Then, for all mesh nodes  $\{\mathbf{x}_j\}_j$  the equation (13) can be reformulated as

$$\mathbf{U}_j^{n+1} = \mathbf{U}_h^{n+1}(\mathbf{x}_j) = \mathbf{U}_h^n(\chi_j^n) := \hat{\mathbf{U}}_j^n, \quad C_j^{n+1} = C_h^{n+1}(\mathbf{x}_j) = C_h^n(\chi_j^n) := \hat{C}_j^n, \quad (19)$$

where  $\hat{\mathbf{U}}_j^n$  and  $\hat{C}_j^n$  are a short notations of  $\mathbf{U}_h^n(\chi_j^n)$  and  $C_h^n(\chi_j^n)$ , respectively. Therefore, the conventional semi-Lagrangian finite element solutions of (5) can be expressed as

$$\mathbf{U}_h^{n+1}(\mathbf{x}) = \sum_{j=1}^{M_v} \hat{\mathbf{U}}_j^n \phi_j(\mathbf{x}), \quad C_h^{n+1}(\mathbf{x}) = \sum_{j=1}^{M_v} \hat{C}_j^n \phi_j(\mathbf{x}). \quad (20)$$

Note that, the precision of the conventional semi-Lagrangian finite element approach depends on the size of the computational mesh utilized in the numerical simulations. Furthermore, it has been demonstrated in<sup>33</sup> that the conventional semi-Lagrangian finite element approach fails to properly handle the steep gradients exhibited by convective components if the computational mesh is not fine enough. In order to overcome such problems, the suggested methodology in the present study is to incorporate local enrichments using the  $L^2$ -projection. This would enhance the accuracy of the semi-Lagrangian finite element solution.

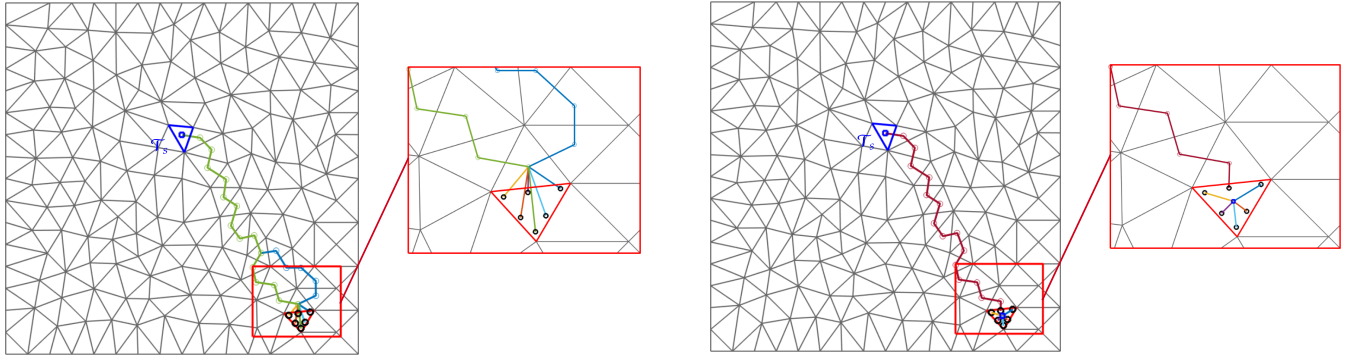


**Figure 3** Illustration of the search-locate algorithm used in<sup>17,18,19</sup> (left plot) and the modified search-locate algorithm adopted in the present study (right plot).

---

**Algorithm 2** Modified search-locate algorithm

---

- 1: **for** each element  $\mathcal{T}_e$  **do**
  - 2:     Chose an arbitrary point  $\mathbf{p}^0 = (p^0, q^0)^\top$  in the reference element  $\mathcal{T}^*$
  - 3:     Select an initial guess for the host element  $\mathcal{T}_s$
  - 4:     **for** each departure point  $\chi_{q,k}$  **do**
  - 5:         Find the mapping  $\mathcal{F}_s$  from  $\mathcal{T}^*$  to  $\mathcal{T}_s$
  - 6:         Compute  $\mathbf{p}^* = (p^*, q^*)^\top$  the solution of equation (17)
  - 7:         **if**  $\mathbf{p}^*$  in  $\mathcal{T}^*$  **then**
  - 8:             The host element  $\hat{\mathcal{T}}_{q,k}$  of  $\chi_{q,k}$  is  $\mathcal{T}_s$ . (i.e.  $\hat{\mathcal{T}}_j \equiv \mathcal{T}_s$ )
  - 9:             Stop
  - 10:         **else**
  - 11:             Apply the selection criteria to select a neighbor elements
  - 12:             Go to step 5
  - 13:         **end if** Select  $\hat{\mathcal{T}}_{q,k}$  as initial guess Go to step 4;
  - 14:     **end for**
  - 15: **end for**
- 

### 3.2 | $L^2$ -projection for local enrichments

In this section, we provide a novel enrichment approach for semi-Lagrangian finite element solution of convection-dominated flow problems based on the  $L^2$ -projection investigated in<sup>35,33</sup>. For simplicity purpose, the suggested approach is formulated only for the concentration solution, and with the same implementation, the velocity solution can be determined. Therefore, the second part of the equation (19) can be written as

$$C_h^{n+1}(\mathbf{x}_j) = C_h^n(\chi_j^n). \quad (21)$$

Thus, multiplying both sides of equation (21) by the finite element basis functions  $\phi_i$  and integrating over  $\Omega$  yields

$$\int_{\Omega} C_h^{n+1}(\mathbf{x}) \phi_i(\mathbf{x}) d\mathbf{x} = \int_{\Omega} C_h^n(\chi_j^n) \phi_i(\mathbf{x}) d\mathbf{x}, \quad i = 1, \dots, M_v. \quad (22)$$

Therefore, the equation (22) can be assembled in a global matrix-vector structure as

$$[\mathbf{M}] \{ \mathbf{C}^{n+1} \} = \{ \mathbf{r}^n \}, \quad (23)$$

where  $[\mathbf{M}]$  is the finite element mass matrix with inputs  $m_{ij} = \int_{\Omega} \phi_j \phi_i d\mathbf{x}$ ,  $\mathbf{C}^{n+1}$  is the vector of the unknown nodal solutions  $C_j^{n+1}$  and  $\mathbf{r}^n$  is the right-hand side vector with entries  $r_i^n$  defined as

$$r_i^n = \int_{\Omega} C_h^n(\chi^n) \phi_i(\mathbf{x}) d\mathbf{x}. \quad (24)$$

To evaluate the integrals  $\{r_i^n\}$  in equation (24), a quadrature rule is used as follows

$$r_i^n = \sum_{k=1}^{N_e} \int_{\mathcal{T}_k} C_h^n(\chi^n) \phi_i(\mathbf{x}) d\mathbf{x} \approx \sum_{k=1}^{N_e} \sum_{q=1}^{N_{k,Q}} \omega_{q,k} C_h^n(\chi_{q,k}^n) \phi_i(\mathbf{x}_{q,k}), \quad (25)$$

where  $\mathbf{x}_{q,k} = (x_{q,k}, y_{q,k})^\top$  are the quadrature points associated with the element  $\mathcal{T}_k$ ,  $\omega_{q,k}$  its corresponding weight,  $N_e$  is the total number of elements in computational mesh,  $N_{k,Q}$  is the total number of quadrature points in the element  $\mathcal{T}_k$ , and  $\chi_{q,k}^n$  is the departure point that will attain the point  $\mathbf{x}_{q,k}$  at time  $t_{n+1}$ . Moreover,  $C_h^n(\chi_{q,k}^n)$  is the concentration solution evaluated at the departure point  $\chi_{q,k}^n$  through the equation (18) as

$$\hat{C}_{q,k}^n := C_h^n(\chi_{q,k}^n) = \sum_{i=1}^N C_h^n(\hat{\mathbf{x}}_i) \varphi_i(\chi_{q,k}^n), \quad q = 1, \dots, N_{k,Q}, \quad (26)$$

where  $\{\hat{\mathbf{x}}_i\}_{i=1}^N$  are the vertices of the element  $\hat{\mathcal{T}}_{q,k}$  hosting  $\chi_{q,k}^n$  and  $\{\varphi_i\}_{i=1}^N$  are their corresponding local basis functions. Therefore, the entries  $m_{ij}$  and  $r_i^n$  in (23) are evaluated as

$$m_{ij} \approx \sum_{k=1}^{N_e} \sum_{q=1}^{N_{k,Q}} \omega_{q,k} \phi_j(\mathbf{x}_{q,k}) \phi_i(\mathbf{x}_{q,k}), \quad r_i^n \approx \sum_{k=1}^{N_e} \sum_{q=1}^{N_{k,Q}} \omega_{q,k} \hat{C}_{q,k}^n \phi_i(\mathbf{x}_{q,k}), \quad i, j = 1, \dots, M. \quad (27)$$

Similarly, the velocity field approximation can be written as

$$[\mathbf{M}] \{ \mathbf{U}^{n+1} \} = \{ \mathbf{z}^n \}, \quad (28)$$

where  $\mathbf{U}^{n+1}$  is the vector of the unknown nodal solutions with entries  $\mathbf{U}_j^{n+1} = (U_j^{n+1}, V_j^{n+1})^\top$  and  $\mathbf{z}^n$  is the right-hand side with inputs  $z_i^n$  calculated in a similar manner as in (25) with

$$z_i^n \approx \sum_{k=1}^{N_e} \sum_{q=1}^{N_{k,Q}} \omega_{q,k} \hat{\mathbf{U}}_{q,k}^n \phi_i(\mathbf{x}_{q,k}), \quad j = 1, \dots, M, \quad (29)$$

where  $\hat{\mathbf{U}}_{q,k}^n = \mathbf{U}_h^n(\chi_{q,k}^n)$  is the velocity solution calculated using (26) at the departure point  $\chi_{q,k}^n$ . Note that the search-locate algorithm used in<sup>17,18,19</sup> is accurate and suitable for the conventional semi-Lagrangian method. However, in our current enriched method for each quadrature point in each element, we compute the corresponding departure point. Although this algorithm converges in few iterations, the use of high number of enrichment makes the search-locate algorithm very demanding. This is mainly because all departure points should be traced starting from an initial guess for the host element as illustrated in the left plot of Figure 3. In this plot, we show the paths followed by the search-locate algorithm to trace the six quadrature points of an element starting from an arbitrary initial guess  $\mathcal{T}_s$ . It can be seen from this figure that for each point there is a considerable number of elements that must be tested before finding the correct host element. Moreover, when high numbers of enrichments are used, tracking departure points using the considered algorithm requires more time which affect the efficiency of the developed approach. In the current work, the search-locate Algorithm 1 is enhanced to improve the efficiency of our method. Since in our enriched method, we search for departure points of a set of quadrature points of a considered element, these departure points must fall in the same element or in elements that are neighbors. Thus, we can trace one of the points using the old search-locate algorithm, then use its host element as an initial guess to search for the rest of departure points as shown in the right plot of Figure 3. Consequently, for a number of enrichments  $N_{k,Q} = 70$ , the new algorithm would find the first point after several iterations, and the other 69 points after one or two iterations maximum. For completeness, the modified search-locate algorithm is detailed in Algorithm 2.

In conclusion, the enriched semi-Lagrangian finite element approach is implemented for advection problem (1) using the steps outlined in Algorithm 3. In this study, the quadrature rules established in<sup>36</sup> are employed. Figure 4 depicts the distribution of the considered quadrature points with  $N_{k,Q} = 6, 12, 25, 52$  and 70. Note that the current study interprets equations (27) as an

**Algorithm 3** Enriched semi-Lagrangian finite element algorithm for the coupled problem.

- 1: Generate the quadrature pair  $(\mathbf{x}_{q,k}, \omega_{q,k})$ ,  $q = 1, \dots, N_{k,Q}$ , and  $k = 1, \dots, N_e$
- 2: Calculate the  $L^2$ -projection mass matrix  $[\mathbf{M}]$  using (27)
- 3: **while**  $t_{n+1} \leq T$  **do**
- 4: Assuming that the approximated solutions  $\mathbf{U}_h^n$  and  $C_h^n$  are known
  - Step 1: Solve the Navier-Stokes equations**
  - 5: **for** each element  $\mathcal{T}_k$  **do**
  - 6: **for** each quadrature point  $\mathbf{x}_{q,k}$ ,  $q = 1, \dots, N_{k,Q}$  **do**
  - 7: Compute the departure point  $\chi_{q,k}^n$  by solving (7)
  - 8: Identify the host element  $\hat{\mathcal{T}}_{q,k}$  where  $\chi_{q,k}^n$  belongs using Algorithm 2
  - 9: Approximate the value of  $\hat{U}_{q,k}^n$  using (26)
  - 10: **end for**
  - 11: **end for**
  - 12: Evaluate the right-hand side entries  $z_i^n$  using (27)
  - 13: Assemble the right-hand side vector  $\mathbf{z}^n$
  - 14: Solve the associated linear system (28)
  - 15: Solve the Stokes problem (6) using Algorithm 3.3
  - 16: Update the velocity field  $\mathbf{U}_h^{n+1}$  at time  $t_{n+1}$  using (4)
  - Step 2: Solve the transport equation**
  - 18: **for** each element  $\mathcal{T}_k$  **do**
  - 19: **for** each quadrature point  $\mathbf{x}_{q,k}$ ,  $q = 1, \dots, N_{k,Q}$  **do**
  - 20: Calculate the departure point  $\chi_{q,k}^n$  by solving (7) using the approximated velocity  $\mathbf{U}_h^{n+1}$
  - 21: Identify the host element  $\hat{\mathcal{T}}_{q,k}$  where  $\chi_{q,k}^n$  belongs using Algorithm 3.3
  - 22: Approximate the value of  $\hat{C}_{q,k}^n$  according to (26)
  - 23: **end for**
  - 24: **end for**
  - 25: Evaluate the right-hand side entries  $r_i^n$  using (27)
  - 26: Assemble the right-hand side vector  $\mathbf{r}^n$
  - 27: Solve the associated linear system (23)
  - 28: Update the concentration  $C_h^{n+1}$  at time  $t_{n+1}$
  - 29: **end while**

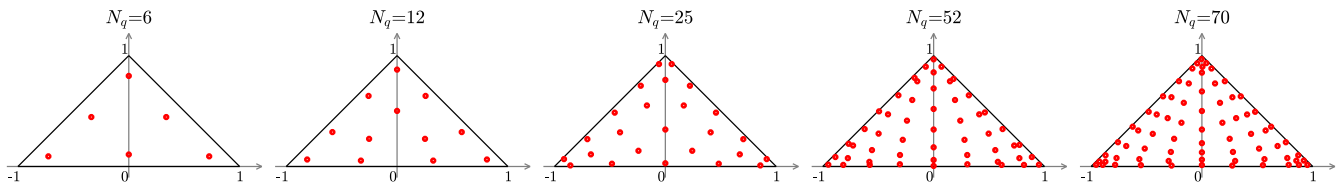


**Figure 4** Distribution of Dunavant quadrature points employed for global and local enrichments.

enrichment approach based on the distribution of quadrature points in the computational mesh. As a result, as stated in section 5, the number of quadrature points  $N_{k,Q}$  can be adjusted globally throughout the whole computational grid or locally at each element. It should be noted that no linear systems of algebraic equations are solved in the conventional Galerkin-characteristic finite element method, and the numerical solution is interpolated using the quadratic shape functions of the element where the departure points  $\chi_i^n$  reside. However, the proposed semi-Lagrangian finite element method, in contrast to the conventional approach, evaluates the departure points  $\chi_{q,k}^n$  for all quadrature points belonging to each triangle  $\mathcal{T}_k$  in the considered grid and

needs a linear system solution to update the numerical solution. It should be noted that alternative quadrature rules may be applied in our approach as well.

### 3.3 | Solution of the Stokes problem

To solve the Stokes problem (6), we formulate the coupled projection scheme based on a rotational pressure correction with a BDF2 time integration method as those studied in<sup>22</sup>. Thus, we solve the Stokes problem (6) for updating the velocity field and pressure at every step using the coupled projection scheme in order to complete the implementation of semi-Lagrangian finite element approach for solving incompressible Navier-Stokes equations (1). Comparing to the standard projection methods, the presence of previous gradient step in the velocity prediction problem improves the order of the scheme. Moreover, the rotational pressure correction projection enhanced the method to avoid artificial boundary conditions on the pressure and improves its rate of convergence<sup>22</sup>. Hence, assuming that  $\hat{\mathbf{U}}^n$ ,  $\hat{\mathbf{U}}^{n-1}$ ,  $\hat{\mathbf{C}}^n$ ,  $\hat{\mathbf{C}}^{n-1}$  and  $p^n$  are known, the Stokes equations (6) are solved using the following steps:

1. Solve for  $C^{n+1} \in \mathbf{V}_h$

$$\frac{3}{2\Delta t} C^{n+1} - \nabla \cdot (D\nabla C^{n+1}) = -\frac{4}{2\Delta t} \hat{\mathbf{C}}^n + \frac{1}{2\Delta t} \hat{\mathbf{C}}^{n-1} + S^n. \quad (30)$$

2. Solve for  $\tilde{\mathbf{U}}^{n+1} \in \mathbf{V}_h$

$$\begin{aligned} \frac{3}{2\Delta t} \tilde{\mathbf{U}}^{n+1} - \nu \Delta \tilde{\mathbf{U}}^{n+1} + \gamma \tilde{\mathbf{U}}^{n+1} - f \left( \tilde{\mathbf{U}}^{n+1} \right)^\top - \beta (C^{n+1} - C_\infty) \mathbf{e} = & \frac{4}{2\Delta t} \hat{\mathbf{U}}^n - \frac{1}{2\Delta t} \hat{\mathbf{U}}^{n-1} \\ & - \nabla p^n + \frac{\tau}{H}. \end{aligned} \quad (31)$$

3. Perform the projection step and compute  $\varphi$  by solving the Poisson problem

$$\Delta \varphi = \frac{3}{2\Delta t} \nabla \cdot \tilde{\mathbf{U}}^{n+1}. \quad (32)$$

4. Velocity correction:

$$\mathbf{U}^{n+1} = \tilde{\mathbf{U}}^{n+1} - \frac{2\Delta t}{3} \nabla \varphi. \quad (33)$$

5. Pressure correction

$$p^{n+1} = p^n + \varphi - \nu \nabla \cdot \tilde{\mathbf{U}}^{n+1}. \quad (34)$$

It should be stressed that in equations (30)-(31), the solutions  $\hat{\mathbf{C}}^{n-1}$ ,  $\hat{\mathbf{C}}^n$ ,  $\tilde{\mathbf{U}}^n$  and  $\tilde{\mathbf{U}}^{n-1}$  are required to advance the solution  $C_h^{n+1}$  and the iterated velocity  $\mathbf{U}_h^{(k)}$  in time. In this case, only one initial condition is given at time  $t = 0$ , and the implicit Euler scheme is used to get the second condition.

## 4 | MULTILEVEL ADAPTIVE ENRICHMENTS

In many applications in coupled flow-transport problems, the Reynolds number reaches high values for which steep gradients, localized eddies and boundary shear layers occur in their numerical solutions. To accurately capture these features, the enriched semi-Lagrangian finite element technique described in section 2 requires very fine meshes and a large number of quadrature points, especially in regions where the values of the solution gradients are very high. In the present study, to avoid uniform enrichments in the entire computational domain, we propose a multilevel adaptive algorithm for local enrichments to increase the efficiency of the proposed method. The key idea in this multilevel adaptive technique lies on refining the number of quadrature points  $N_{k,Q}$  in mesh elements where the solution gradient generates high values and unrefine otherwise according to a given adaptation criterion. In practice, an error indicator and a specified tolerance are needed to adjust the quadrature at each time step. For example, gradient-based error estimators have been widely used in the literature in  $h$ -adaptive finite element methods for solving incompressible Navier-Stokes equations, see<sup>23,24,25,26,27,28,29</sup> among others. However, most of these gradient-based  $h$ -adaptive techniques use an initial coarse mesh to compute a primary solution for estimating the gradient errors. Consequently, an accumulation of errors in time is expected due to the coarse mesh used in the approximation and also the computational cost

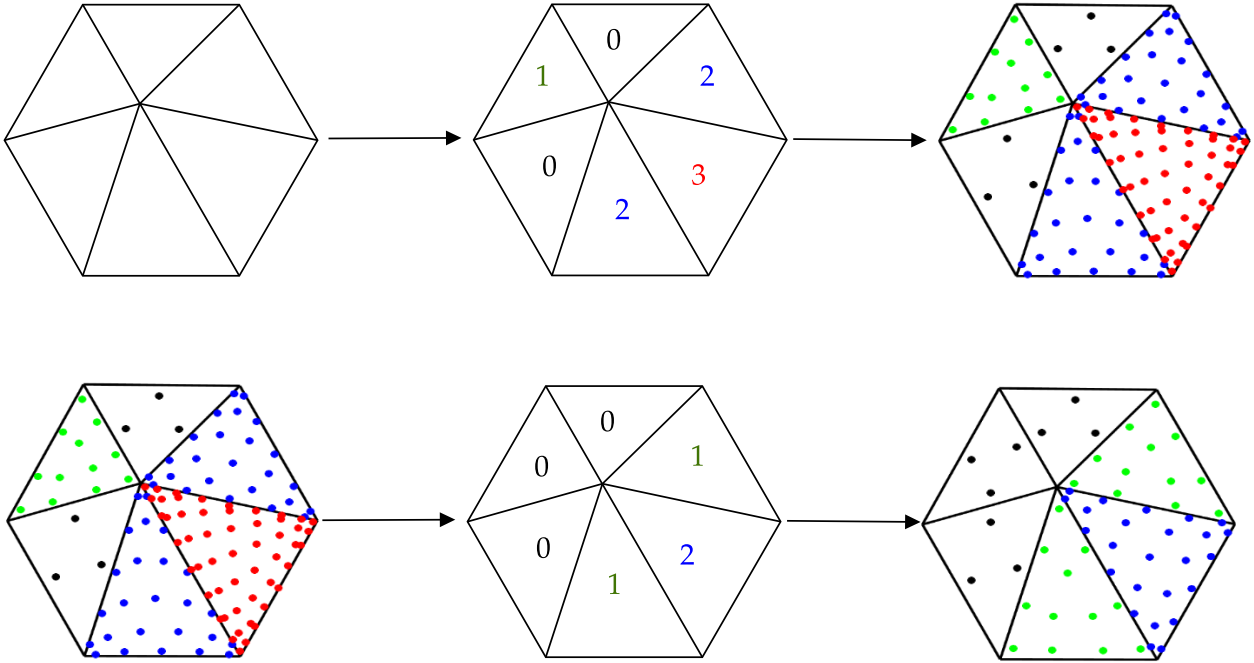


**Figure 5** Schematic description of refinement (top plot) and unrefinement (bottom plot) used for multilevel adaptive enrichments.

becomes prohibitive due to multiple interpolations between adaptive meshes. In the current work, we consider the normalized gradient of the concentration as an adaptive criterion for the local enrichments of each element in the computational domain defined by

$$err^{n+1}(\mathcal{T}_k) = \frac{\|\nabla C_{\mathcal{T}_k}^{n+1}\|}{\max_{j=1}^{N_e} \|\nabla C_{\mathcal{T}_j}^{n+1}\|}, \quad (35)$$

where  $C_{\mathcal{T}_k}^{n+1}$  is the concentration on the triangle  $\mathcal{T}_k$  at time  $t_{n+1}$  and  $\|\nabla C_{\mathcal{T}_k}^{n+1}\|$  is the  $L^2$ -norm of the gradient of the solution on  $\mathcal{T}_k$  defined by

$$\|\nabla C_{\mathcal{T}_k}^{n+1}\| = \sqrt{\int_{\mathcal{T}_k} \nabla C_{\mathcal{T}_k}^{n+1} \cdot \nabla C_{\mathcal{T}_k}^{n+1} d\Omega}. \quad (36)$$

The considered error indicator (35) can benefit from the semi-Lagrangian method to approximate the gradient  $\|\nabla C_{\mathcal{T}_k}^{n+1}\|$  backwards in time from the known solution at time  $t_n$ . Thus, applying the gradient to the restriction of the solution (20) on the element  $\mathcal{T}_k$  we obtain

$$\nabla C_{\mathcal{T}_k}^{n+1} = \sum_{i=1}^N \hat{C}_i^n \nabla \varphi_i. \quad (37)$$

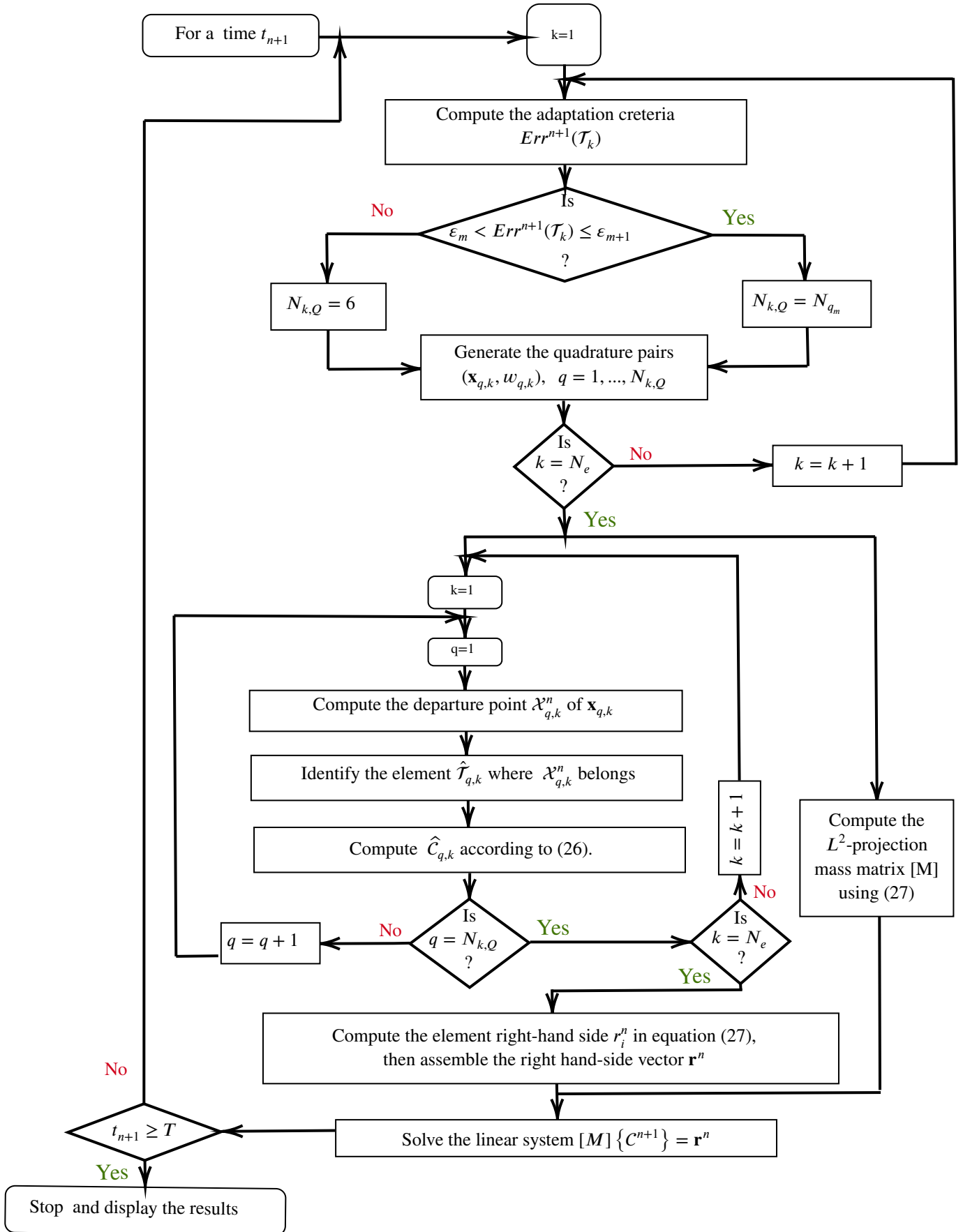


Figure 6 Adaptive enriched semi-Lagrangian finite element flowchart.

Therefore, the integral in (36) can be evaluated as

$$\begin{aligned}
\|\nabla C_{\mathcal{T}_k}^{n+1}\| &= \sqrt{\int_{\mathcal{T}_k} \nabla C_{\mathcal{T}_k}^{n+1} \cdot \nabla C_{\mathcal{T}_k}^{n+1} d\Omega}, \\
&= \sqrt{\int_{\mathcal{T}_k} \left( \sum_{i=1}^N \hat{C}_i^n \nabla \varphi_i \right) \cdot \left( \sum_{j=1}^N \hat{C}_j^n \nabla \varphi_j \right) d\Omega}, \\
&= \sqrt{\sum_{i=1}^N \hat{C}_i^n \left( \sum_{j=1}^N \hat{C}_j^n \int_{\mathcal{T}_k} \nabla \varphi_i \cdot \nabla \varphi_j d\Omega \right)}, \\
&= \sqrt{\left( \hat{C}_{\mathcal{T}_k}^n \right)^\top \mathbf{S}_{\mathcal{T}_k} \hat{C}_{\mathcal{T}_k}^n}. \tag{38}
\end{aligned}$$

where  $\hat{C}_{\mathcal{T}_k}^n = (\hat{C}_1^n, \dots, \hat{C}_N^n)^\top$  are the solutions values computed at the departure points of the vertices of the element  $\mathcal{T}_k$  at time  $t_n$ , and  $\mathbf{S}_{\mathcal{T}_k}$  denotes the elementary stiffness matrix associated with the element  $\mathcal{T}_k$ . Normalizing the error indicator is a very important task in our case as ensures that criteria (35) is recognized to take values between 0 and 1. As a result, the multilevel adaptation method we suggest in this work is carried out in the following manner:

Assuming that the values for the tolerances  $\{\varepsilon_m\}$  satisfy  $0 = \varepsilon_0 < \varepsilon_1 < \varepsilon_2 < \varepsilon_3 < \varepsilon_4 = 1$ . If an element of the mesh  $\mathcal{T}_k$  meets the following criteria

$$\varepsilon_m \leq \text{err}^{n+1}(\mathcal{T}_k) \leq \varepsilon_{m+1}, \quad 0 \leq m \leq 3,$$

then  $\mathcal{T}_k$  is enriched using the quadrature pairs  $(\mathbf{x}_{k,q}, w_{k,q})$  with  $q = 1, 2, \dots, N_{k,q_m}$ . It should be noted that the values of tolerances  $\{\varepsilon_m\}$  and the number of levels vary depending on the addressed problem, and their explanation is deferred until section 5 which includes numerical test cases. The suggested adaptive enriched semi-Lagrangian finite element technique for solving the convection phase is described in flowchart displayed in Figure 6.

## 5 | NUMERICAL RESULTS

In this section, the accuracy of the new enriched semi-Lagrangian finite element method introduced in the above sections is assessed using test examples of incompressible flow problems. This is expected to ensure the robustness of the proposed methodology before applying it for the real case of transport and dispersion of phosphogypsum in the Jorf Lasfar coastal zone. For this reason a test example with known analytical solution is considered. Consequently, the relative  $L^1$ -error and  $L^2$ -error at time  $t_n$  can be evaluated, such that

$$L^1\text{-error} = \frac{\int_{\Omega} |U_h^n - U_{\text{exact}}^n| d\Omega}{\int_{\Omega} |U_{\text{exact}}^n| d\Omega}, \quad L^2\text{-error} = \frac{\left( \int_{\Omega} |U_h^n - U_{\text{exact}}^n|^2 d\Omega \right)^{\frac{1}{2}}}{\left( \int_{\Omega} |U_{\text{exact}}^n|^2 d\Omega \right)^{\frac{1}{2}}}, \tag{39}$$

where  $U_{\text{exact}}^n$  and  $U_h^n$  are respectively, the exact and numerical solutions obtained at the gridpoint  $\mathbf{x}_h$  and time  $t_n$ . In all the computations reported in this section, resulting linear systems of algebraic equations are solved using the conjugate gradient solver with incomplete Cholesky decomposition. In addition, all stopping criteria for iterative solvers were set to  $10^{-6}$ , which is small enough to guarantee that the algorithm truncation error dominates the total numerical error. All the computations are performed on an Intel® Core(TM) i7-7500U @ 2.70GHz with 16 GB of RAM.

### 5.1 | Transport problem with anisotropic dispersion

The main purpose of this test example is to demonstrate the performance of the novel adaptive enriched semi-Lagrangian finite element approach for handling anisotropic advection-diffusion problems. For this reason, only the convection-diffusion equations

**Table 1** Results for the transport problem with anisotropic dispersion obtained using the enriched semi-Lagrangian finite element method with both adaptive and fixed enrichments on structured meshes using different quadratures and anisotropy parameters.

$\alpha_L = 10$ and $\alpha_T = 10^{-1}$													
$h$	$N_Q$	Fixed enrichments						Adaptive enrichments					
		$L^1$ -error	$L^2$ -error	Mass	Max $C$	Min $C$	CPU	$L^1$ -error	$L^2$ -error	Mass	Max $C$	Min $C$	CPU
$\frac{1}{32}$	12	4.759E-02	4.320E-02	0.996	0.6082	-0.0033	0.93	4.823E-02	4.320E-02	0.996	0.6082	-0.0033	0.76
	25	2.568E-02	2.080E-02	0.996	0.5862	-0.0025	1.55	2.574E-02	2.138E-02	0.996	0.5865	-0.0025	0.99
	52	1.867E-02	1.469E-02	0.997	0.5745	-0.0008	2.39	1.889E-02	1.470E-02	0.997	0.5745	-0.0008	1.32
	70	1.336E-02	1.078E-02	0.997	0.5720	-0.0003	3.30	1.424E-02	1.124E-02	0.997	0.5721	-0.0004	1.45
$\frac{1}{64}$	12	8.429E-03	5.755E-03	0.998	0.5741	-0.0001	3.98	8.425E-03	5.755E-03	0.998	0.5741	-0.0001	1.94
	25	5.914E-03	4.781E-03	0.999	0.5717	0.0000	5.35	5.954E-03	4.781E-03	0.999	0.5717	0.0000	2.21
	52	3.194E-03	2.544E-03	0.999	0.5710	0.0000	8.45	3.356E-03	2.551E-03	0.999	0.5710	0.0000	2.78
	70	2.757E-03	2.411E-03	0.999	0.5708	0.0000	12.36	2.834E-03	2.417E-03	0.999	0.5708	0.0000	3.61
$\frac{1}{128}$	12	1.220E-03	1.106E-03	0.999	0.5708	0.0000	13.54	1.222E-03	1.106E-03	0.999	0.5708	0.0000	6.59
	25	9.384E-04	6.455E-04	0.999	0.5704	0.0000	23.04	9.384E-04	6.455E-04	0.999	0.5704	0.0000	7.38
	52	8.264E-04	5.573E-04	1.000	0.5701	0.0000	37.30	8.266E-04	5.573E-04	1.000	0.5701	0.0000	11.77
	70	6.188E-04	4.155E-04	1.000	0.5700	0.0000	48.81	6.208E-04	4.155E-04	1.000	0.5700	0.0000	14.16
$\alpha_L = 10^{-1}$ and $\alpha_T = 10$													
$h$	$N_Q$	Fixed enrichments						Adaptive enrichments					
		$L^1$ -error	$L^2$ -error	Mass	Max $C$	Min $C$	CPU	$L^1$ -error	$L^2$ -error	Mass	Max $C$	Min $C$	CPU
$\frac{1}{32}$	12	2.342E-01	1.828E-01	0.997	0.5168	-0.0219	0.92	2.344E-01	1.828E-01	0.997	0.5168	-0.0219	0.74
	25	8.946E-02	7.608E-02	0.998	0.5174	-0.0107	1.53	9.014E-02	7.608E-02	0.997	0.5174	-0.0107	0.98
	52	6.477E-02	5.717E-02	0.998	0.5353	-0.0082	2.39	6.477E-02	5.717E-02	0.998	0.5353	-0.0082	1.33
	70	5.118E-02	4.240E-02	0.999	0.5534	-0.0037	3.27	5.106E-02	4.239E-02	0.999	0.5534	-0.0037	1.40
$\frac{1}{64}$	12	2.594E-02	2.396E-02	0.998	0.5784	-0.0011	3.95	2.600E-02	2.396E-02	0.998	0.5784	-0.0011	1.90
	25	9.893E-03	8.585E-03	0.999	0.5744	0.0000	5.35	9.952E-03	8.586E-03	0.999	0.5744	0.0000	2.19
	52	7.364E-03	6.757E-03	0.999	0.5713	0.0000	8.44	7.593E-03	6.758E-03	0.999	0.5713	0.0000	2.75
	70	5.502E-03	4.832E-03	1.000	0.5702	0.0000	12.56	5.594E-03	4.833E-03	1.000	0.5702	0.0000	3.61
$\frac{1}{128}$	12	4.183E-03	2.841E-03	0.999	0.5710	0.0000	13.52	4.201E-03	2.842E-03	0.999	0.5710	0.0000	6.60
	25	2.363E-03	1.588E-03	1.000	0.5702	0.0000	23.34	2.381E-03	1.593E-03	1.000	0.5702	0.0000	7.36
	52	1.651E-03	1.503E-03	1.000	0.5699	0.0000	37.00	1.662E-03	1.503E-03	1.000	0.5699	0.0000	11.16
	70	9.813E-04	6.317E-04	1.000	0.5699	0.0000	49.09	9.890E-04	6.321E-04	1.000	0.5699	0.0000	14.29
$\alpha_L = 10$ and $\alpha_T = 10$													
$h$	$N_Q$	Fixed enrichments						Adaptive enrichments					
		$L^1$ -error	$L^2$ -error	Mass	Max $C$	Min $C$	CPU	$L^1$ -error	$L^2$ -error	Mass	Max $C$	Min $C$	CPU
$\frac{1}{32}$	12	3.733E-02	3.673E-02	0.997	0.3355	-0.0002	1.10	3.745E-02	3.674E-02	0.997	0.3355	-0.0002	0.82
	25	9.620E-03	7.894E-03	0.997	0.3210	-0.0001	1.64	9.626E-03	7.892E-03	0.997	0.3210	-0.0001	0.99
	52	7.546E-03	6.198E-03	0.998	0.3172	0.0000	2.59	7.556E-03	6.197E-03	0.998	0.3172	0.0000	1.36
	70	5.660E-03	4.843E-03	0.999	0.3140	0.0000	3.53	5.679E-03	4.842E-03	0.999	0.3140	0.0000	1.42
$\frac{1}{64}$	12	3.674E-03	2.696E-03	0.998	0.3146	0.0000	4.14	3.687E-03	2.699E-03	0.998	0.3146	0.0000	1.92
	25	2.127E-03	1.634E-03	0.999	0.3142	0.0000	5.49	2.152E-03	1.637E-03	0.999	0.3142	0.0000	2.21
	52	8.946E-04	6.197E-04	0.999	0.3138	0.0000	9.05	8.953E-04	6.197E-04	0.999	0.3138	0.0000	2.78
	70	7.649E-04	5.023E-04	1.000	0.3137	0.0000	12.62	7.676E-04	5.024E-04	1.000	0.3137	0.0000	3.64
$\frac{1}{128}$	12	5.696E-04	4.038E-04	0.999	0.3143	0.0000	14.36	5.720E-04	4.040E-04	0.999	0.3143	0.0000	6.62
	25	3.246E-04	2.343E-04	1.000	0.3137	0.0000	24.43	3.269E-04	2.346E-04	1.000	0.3137	0.0000	7.47
	52	2.671E-04	2.066E-04	1.000	0.3135	0.0000	37.82	2.690E-04	2.068E-04	1.000	0.3135	0.0000	11.20
	70	1.698E-04	1.796E-04	1.000	0.3135	0.0000	49.97	1.711E-04	1.798E-04	1.000	0.3135	0.0000	14.35

in (1) without the source term are considered with a given stationary flow field as

$$\begin{aligned} \frac{\partial C}{\partial t} + \mathbf{U} \cdot \nabla C - \nabla \cdot (\mathbf{D} \nabla C) &= 0, & \text{in } \Omega \times [0, T], \\ C(x, y, t) &= g(x, y, t), & \text{in } \partial\Omega \times [0, T], \\ C(x, y, 0) &= C_0(x, y), & \text{in } \Omega, \end{aligned} \quad (40)$$

where the computational domain  $\Omega = [-1500, 1500] \times [-1500, 1500]$ , the initial condition is defined as

$$C_0(x, y) = \frac{c_0}{2\pi\sigma_0^2} \exp\left(-\frac{(x-x_0)^2 + (y-y_0)^2}{2\sigma_0^2}\right),$$

whereas the boundary function  $g(x, y, t)$  is obtained from the following analytical solution

$$C(x, y, t) = \frac{c_0}{2\pi\sqrt{|\det(\sigma)|}} \exp\left(-\frac{(\bar{\mathbf{x}} - \mathbf{U}t)^\top \sigma^{-1} (\bar{\mathbf{x}} - \mathbf{U}t)}{2}\right), \quad (41)$$

where  $\sigma = \sigma_0^2 \mathbf{I} + 2\mathbf{D}t$ ,  $\sigma^{-1}$  represents the inverse matrix of  $\sigma$ ,  $|\det(\sigma)|$  is the absolute value of the determinant of  $\sigma$ , and  $\mathbf{D}$  is the dispersion tensor given by (2)-(3). In our simulations for this example we set  $c_0 = 150000$ ,  $\sigma_0 = 150$ ,  $D_m = 10^{-3}$ ,  $\bar{\mathbf{x}} = (x - x_0, y - y_0)^\top$ , with  $(x_0 = -1050, y_0 = -1050)$  and the velocity field is assumed stationary given by  $\mathbf{U} = (450, 450)^\top$ . In this test case, the ability of local enrichments to properly reproduce steep gradients in numerical solutions is assessed using different anisotropy corresponding to different values of longitudinal and transverse dispersion coefficients  $\alpha_L$  and  $\alpha_T$ . It is easy to verify, using the definition of the Peclet number  $\frac{\|\mathbf{U}\| L_{ref}}{\|\mathbf{D}\|}$ , that the associated Peclet number for this test example is 300 for all considered values of the dispersion coefficients  $\alpha_L$  and  $\alpha_T$ . As discussed in section 4, the suggested method is accompanied by a multilevel adaptive technique that uses three different tolerance values. For this example, we set  $\varepsilon_1 = 0.07$ ,  $\varepsilon_2 = 0.2$  and  $\varepsilon_3 = 0.3$ . According to these considered values, a three-level enrichment is performed using ( $N_{k,Q} = 70$ ,  $N_{k,Q} = 52$ ,  $N_{k,Q} = 12$ ). The number of quadrature points in elements which are not subject to enrichments we used fixed  $N_{k,Q} = 6$ .

Quantitative results, including the relative  $L^1$ -error and  $L^2$ -error, relative mass (Mass), maximum (Max), minimum (Min) and computational costs (CPU) are summarized in Table 1. These results are computed using the suggested fixed and adaptive enriched semi-Lagrangian finite element method with several structured meshes, quadratures, and different values of  $(\alpha_L, \alpha_T)$ . Table 2 also includes those results obtained using the conventional semi-Lagrangian finite element approach for the same considered parameters. Note that the maximum of the analytical solution is also included in Table 2 whereas, the analytical minimum is 0. Based on the results obtained for  $L^1$ -error and  $L^2$ -error in Table 1, the fixed and adaptive enrichment techniques yield comparable results with minor differences for all meshes and quadrature point counts. The conventional semi-Lagrangian finite element approach, on the other hand, is less accurate than the suggested enriched methods, compare the results in Table 2. In addition, the conventional semi-Lagrangian approach produces negative minimum values, which can be improved by increasing the number of enrichments in the enriched outcomes. When refining the computational mesh or increasing the number of quadrature points in simulations, Table 1 and Table 2 show a clear improvement in the accuracy of the results produced using all the considered numerical methods. Refining the mesh or increasing the quadrature points, for example, enhances the accuracy of the relative mass in Table 1. By comparing results for the computational costs, the fixed enrichment strategy is clearly more expensive than the adaptive enrichment approach. The CPU time needed by the adaptive enriched technique is 63% less than that required by the fixed enriched approach for the parameters evaluated. Moreover, in comparison to the fixed enriched method requirements using a fine mesh with  $\frac{1}{128}$  and  $N_{k,Q} = 70$ , the local enrichments reduced the computational cost by 71%. Finally, although the computational cost of the conventional semi-Lagrangian method is significantly lower compared to the suggested method, the latter presents much higher performance in terms of precision and consistency, see Table 2.

To further illustrate the results listed in Table 1 and Table 2, cross-sections at the main diagonal  $x = y$  of the results computed using fixed and adaptive enrichment approaches at two different times  $t = 0.4$  and  $t = 4.24$  are displayed in Figure 7. Results obtained using the conventional method and the analytical solution are also included in this figure. These results are evaluated on a structured mesh with  $h = \frac{1}{32}$  and various numbers of enrichments  $N_{k,Q} = 12, 25$ , and  $70$  for the anisotropy cases  $(\alpha_L, \alpha_T) = (10, 10^{-1})$ ,  $(\alpha_L, \alpha_T) = (10^{-1}, 10)$  and  $(\alpha_L, \alpha_T) = (10, 10)$ . The accuracy of numerical results generated using the enriched semi-Lagrangian finite element approach with both fixed and adaptive enrichments increases when the number of enrichments  $N_{k,Q}$  is high either globally or locally in the computational mesh, as shown in Figure 7. The results, displayed in the same figure, computed using the traditional semi-Lagrangian technique, indicate excessive numerical diffusion. All of those results were obtained using the same  $P_2$  finite element model.

**Table 2** Results for the transport problem with anisotropic dispersion obtained using the conventional semi-Lagrangian finite element method on structured meshes using different quadratures and anisotropy parameters.

$\alpha_L = 10$ and $\alpha_T = 10^{-1}$							
$h$	$L^1$ -error	$L^2$ -error	Mass	Exact Max	Max $C$	Min $C$	CPU
$\frac{1}{32}$	2.65827E-01	2.42053E-01	1.0509	0.5700	0.4364	-0.0015	0.49
$\frac{1}{65}$	6.00554E-02	5.77386E-02	0.9951	0.5700	0.5311	-0.0003	1.82
$\frac{1}{128}$	1.04466E-02	9.83793E-03	0.9978	0.5700	0.5652	0.0000	7.47
$\frac{1}{256}$	1.75037E-03	1.79344E-03	0.9996	0.5700	0.5705	0.0000	33.56
$\alpha_L = 10^{-1}$ and $\alpha_T = 10$							
$h$	$L^1$ -error	$L^2$ -error	Mass	Exact Max	Max $C$	Min $C$	CPU
$\frac{1}{32}$	6.21264E-01	4.76727E-01	1.0495	0.5699	0.3324	-0.0136	0.48
$\frac{1}{65}$	2.39633E-01	2.10466E-01	1.0038	0.5699	0.4694	-0.0167	1.88
$\frac{1}{128}$	5.95296E-02	5.38938E-02	0.9963	0.5699	0.5492	-0.0016	7.57
$\frac{1}{256}$	2.78376E-03	2.56909E-03	0.9992	0.5699	0.5702	-0.0000	34.28
$\alpha_L = 10$ and $\alpha_T = 10$							
$h$	$L^1$ -error	$L^2$ -error	Mass	Exact Max	Max $C$	Min $C$	CPU
$\frac{1}{32}$	2.09094E-01	1.96180E-01	1.0133	0.3135	0.2593	-0.0020	0.48
$\frac{1}{65}$	4.62392E-02	4.47009E-02	0.9777	0.3135	0.3012	-0.0001	1.80
$\frac{1}{128}$	9.42312E-03	8.89406E-03	0.9829	0.3135	0.3126	0.0000	7.24
$\frac{1}{256}$	9.85869E-04	9.56553E-04	0.9994	0.3135	0.3132	0.0000	33.93

To compare the results obtained by the adaptive and fixed enriched semi-Lagrangian approaches to those computed using the conventional semi-Lagrangian method and the analytical results, we display in Figure 8, 15 equi-distributed contourlines of the computed solution at times  $t = 0.4$  and  $t = 4.24$  using  $N_{k,Q} = 12, 25$  and  $70$  and for  $(\alpha_L = 10^{-1}, \alpha_T = 10)$ . The results obtained using  $(\alpha_L = 10, \alpha_T = 10^{-1})$  and  $(\alpha_L = 10, \alpha_T = 10)$  are displayed in Figure 9 and Figure 10, respectively. From these figures, it can be concluded that when the fixed and adaptive enrichments provide identical results with little variation compared to the analytical solutions, the conventional semi-Lagrangian finite element approach fails to solve the issue, as predicted.

Finally, contourlines of the numerical solution produced by the three-level enrichment technique, its corresponding gradients, and the distribution of quadrature points formed the three-level enrichments at times  $t = 0.6$  and  $t = 4.24$  are illustrated in Figure 11 for  $(\alpha_L = 10^{-1}, \alpha_T = 10)$ ,  $(\alpha_L = 10, \alpha_T = 10^{-1})$  and  $(\alpha_L = 10, \alpha_T = 10)$ . The purpose here is to assess the effectiveness of the adaptive enriched approach in capturing the transport and dispersion feature of a Gaussian pulse on a coarse structured mesh with  $h = \frac{1}{32}$ . The enrichment level for each element in the computational mesh is depicted using a different color. Figure 11 illustrates that the position of the quadrature points for the three-level enrichments capture the solution gradients correctly and that the distribution of these enrichment points has not been distorted. As a result, the investigated adaptive enrichment approach effectively solves the convection-diffusion issue since the mesh is kept constant during the temporal integration operation, allowing for local adjustment of the enrichment points where needed.

## 5.2 | Application to dispersion in the Jorf Lasfar

We turn our attention to the application of the developed numerical tools to simulate the real case of Phosphogypsum release at the Jorf Lasfar industrial platform. The objective here is to assess the robustness of the methodology proposed in this study to resolve the underlying complex transport of the release. The mathematical model (1) is therefore considered to predict the transport and dispersion of Phosphogypsum in the Jorf Lasfar, where  $C$  represents the concentration of Phosphogypsum in the

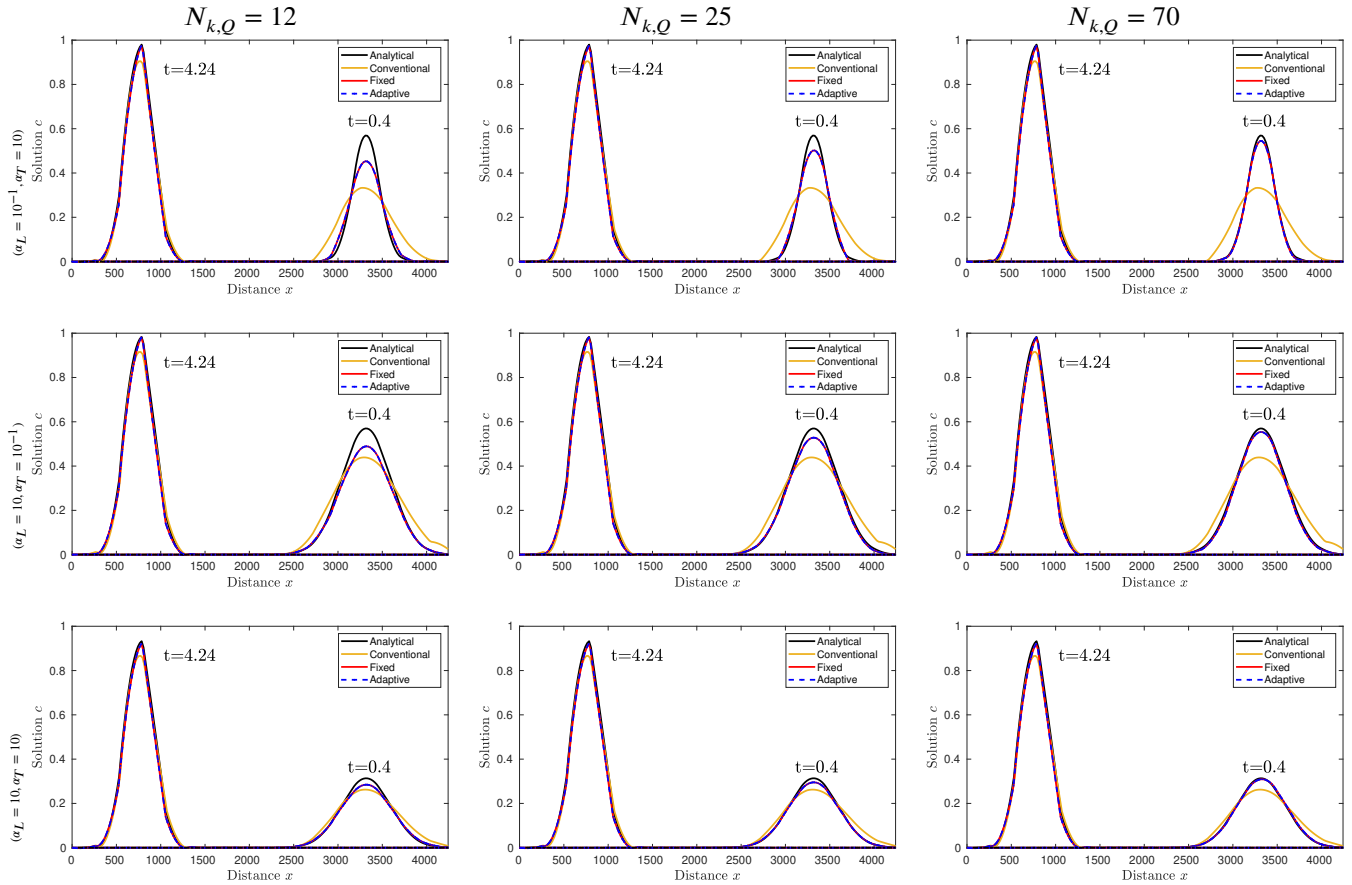


**Figure 7** Cross-sections at the main diagonal  $x = y$  obtained for the transport problem with anisotropic dispersion at two different times  $t = 0.4$  and  $t = 4.24$  on a structured mesh with  $h = \frac{1}{32}$  using  $(\alpha_L = 10^{-1}, \alpha_T = 10)$  (first row),  $(\alpha_L = 10, \alpha_T = 10^{-1})$  (second row) and  $(\alpha_L = 10, \alpha_T = 10)$  (third row) with  $N_{k,Q} = 12$  (first column),  $N_{k,Q} = 25$  (second column) and  $N_{k,Q} = 70$  (third column).

ocean. Note that the use of a Fickian dispersion tensor used in the current work is motivated based on the complex rheological behavior of the phosphate slurry, see for instance<sup>37</sup>. Furthermore, the physical domain is defined through a high-resolution (of 10 m) remote sensing product (Sentinel-2), as depicted by Figure 12. Notice that the dispersion of Phosphogypsum in the ocean is clearly visible in Figure 12, compare the region bounded by the red contourline on the map. Here, the problem statement consists of solving the system (1) in the corresponding domain near the Jorf Lasfar platform. A qualitative calibration of dispersion parameters is performed in order to obtain the same feature observed by the remote sensing product. Following this methodology, the molecular dispersion coefficient  $D_m = 10^{-3} \text{ m}^2/\text{s}$ , the longitudinal dispersion coefficient  $\alpha_L = 5 \times 10^{-2} \text{ m}^2/\text{s}$  and the transverse dispersion coefficient  $\alpha_T = 10^{-2} \text{ m}^2/\text{s}$ . In our simulations, the Coriolis parameter  $f = 8.55 \times 10^{-5} / \text{s}$ , the bottom friction coefficient  $\gamma = 0.012 \text{ s}/\text{m}^{1/3}$ , the coefficient of solute expansion  $\beta = 1$ , the reference concentration  $C_\infty = 0$ , the kinematic viscosity  $\nu = 1.67 \times 10^{-3} \text{ kg}/\text{ms}$  and the wind stress  $\tau = 1.5 \text{ N}/\text{m}^2$  which is equivalent to a wind speed of  $28 \text{ m}/\text{s}$ . It is worth mentioning that, in order to perform a quantitative calibration, further treatments on the satellite products are required as discussed in<sup>38</sup>. However, this is out of the scope in the present work and only the robustness of the model is assessed.

Our main objective in these numerical simulations is twofold, on one hand to demonstrate the performance of the proposed multilevel adaptive enriched semi-Lagrangian finite element method to accurately resolve complex geometries and on the other hand to develop a class of robust computational techniques to efficiently simulate the transport and dispersion of phosphogypsum in the Jorf Lasfar coastal zone. In our computations, we implement a three-level adaptive enrichment with tolerances fixed to  $\epsilon_1 = 0.07$ ,  $\epsilon_2 = 0.13$  and  $\epsilon_3 = 0.3$  for which the initial number of quadrature points is set to  $N_{k,Q} = 6$  in each element and this number is refined accordingly using  $(N_{k,Q} = 12, N_{k,Q} = 25, N_{k,Q} = 52)$ . Here, using the image shown in Figure 12, a computational domain is generated for the equations (1) to be solved subject to a continuous release of  $S = 1.2 \text{ tones}/\text{hour}$

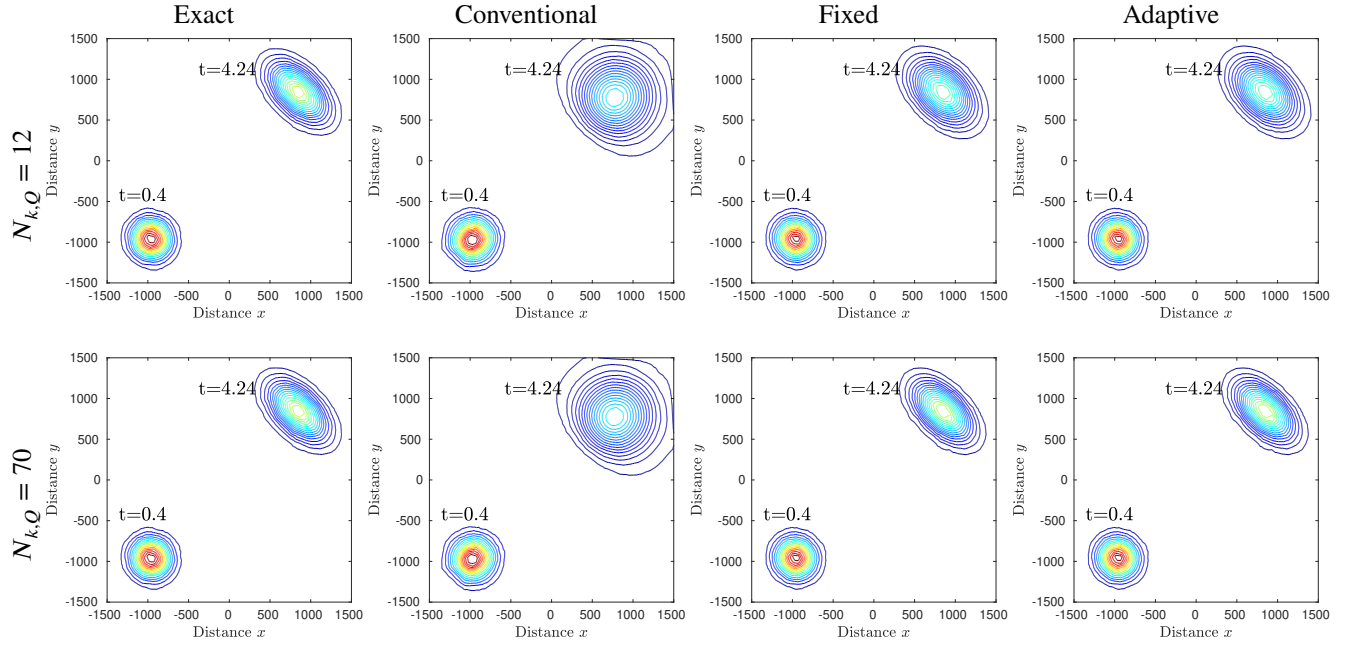


**Figure 8** Results obtained for the transport problem with anisotropic dispersion at two different times  $t = 0.4$  and  $t = 4.24$  on a structured mesh with  $h = \frac{1}{32}$  using  $(\alpha_L = 10^{-1}, \alpha_T = 10)$  for the exact solution (first column), conventional method (second column), fixed enrichments (third column) and adaptive enrichments (fourth column) with  $N_{k,Q} = 12$  (first row) and  $N_{k,Q} = 70$  (second row).

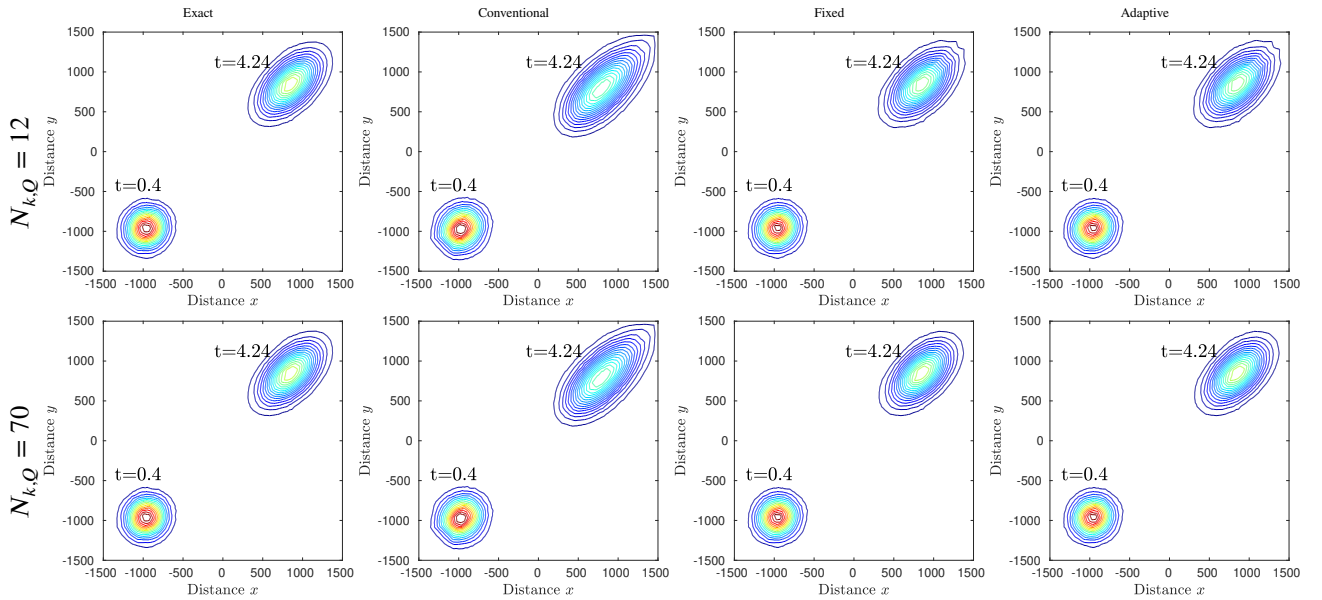


**Figure 9** Same as Figure 8 but using  $(\alpha_l = 10, \alpha_t = 10^{-1})$ .

located at the point  $(11.55 \text{ Km}, 2 \text{ Km})^\top$ . Initially, the system is assumed to be at rest, no-slip boundary conditions are used on the coastlines, and a well developed velocity profile with a maximum velocity  $u_\infty = 0.18 \text{ m/s}$  is imposed at the open water boundaries. Note that this velocity profile corresponds to the annual mean of the Atlantic input flux and it is also comparable to the main semidiurnal component  $M_2$ , see for instance<sup>39</sup>. Notice that for the considered flow conditions and based on the definition of the Reynolds number  $\frac{u_\infty L_{ref}}{\nu}$ , the associated Reynolds number for this problem is about  $5 \times 10^6$ .

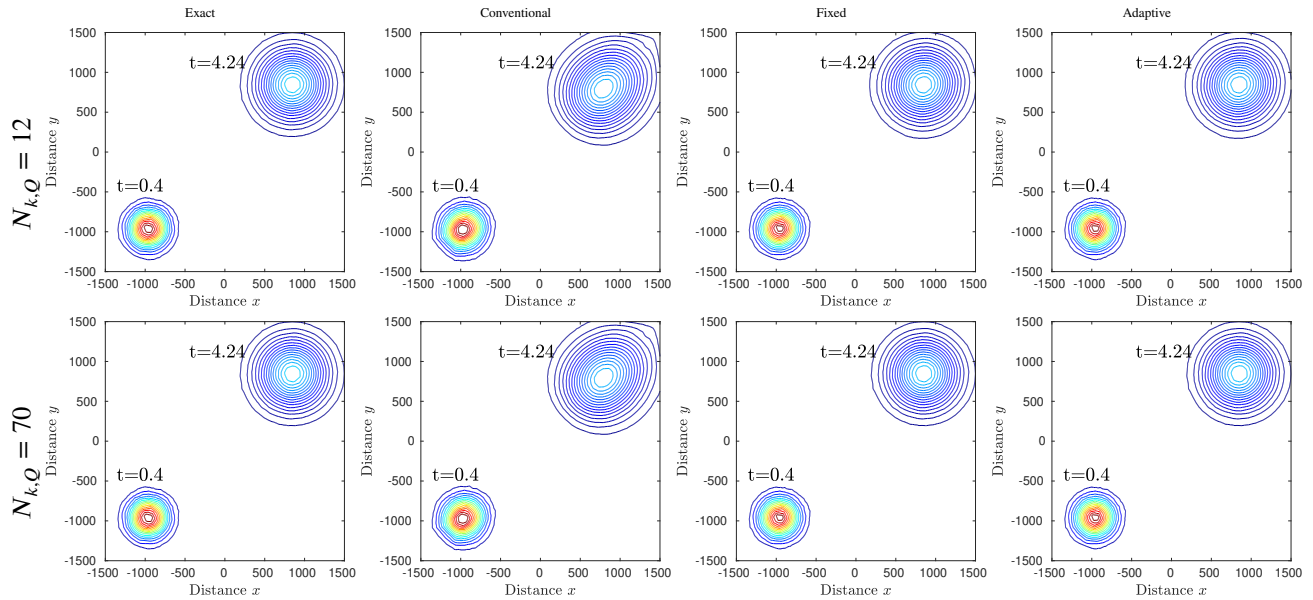


**Figure 10** Same as Figure 8 but using  $(\alpha_l = 10, \alpha_l = 10)$ .

We first perform a mesh convergence study for this problem by considering a series of unstructured meshes as shown in Figure 13 with the corresponding statistics of elements and nodes given in Table 3. Figure 14 depicts the time evolution of the concentration computed at three different gauge stations, G1, G2 and G3 in the Jorf Lasfar as illustrated on the meshes in Figure 13. Here, the selected gauges G1, G2 and G3 are located in the Jorf Lasfar at  $(10.7 \text{ Km}, 4.1 \text{ Km})^\top$ ,  $(10.7 \text{ Km}, 6.5 \text{ Km})^\top$  and  $(11.4 \text{ Km}, 9.4 \text{ Km})^\top$ , respectively. It should be noted that the reference solution is calculated using the fixed method on the reference mesh using  $N_{k,Q} = 70$ . It is clear that the concentrations obtained for the selected gauges using the coarse Mesh I are less accurate than those obtained using Mesh II and Mesh III. Refining the density of elements in the computational domain, results obtained on Mesh II and Mesh III are relatively close. This confirms the mesh convergence in the proposed multilevel adaptive enriched semi-Lagrangian finite element method for this problem. To further quantify the results for this mesh convergence study, we also calculate the total kinetic energy and averaged concentration volume as

$$\frac{1}{2} \int_{\Omega} (U^2(\mathbf{x}, t) + V^2(\mathbf{x}, t)) d\mathbf{x} \quad \text{and} \quad \frac{1}{|\Omega|} \int_{\Omega} C(\mathbf{x}, t) d\mathbf{x}. \quad (42)$$

Table 3 summarizes the averaged concentration volume, computational time, and total kinetic energy produced using the considered meshes at time  $t = 24 \text{ hours}$ . It is evident that minor differences are detected in the values obtained for total kinetic energy and averaged concentration volume on Mesh II, Mesh III, and Reference mesh. Furthermore, differences in the results obtained for total kinetic energy and averaged concentration volume on Mesh II and Reference mesh are less than 2.36% and 3.56%, respectively. On Mesh III and Reference mesh, these values drop to less than 1% and 1.93%, respectively. In addition, the computational time required for the proposed method on Mesh III, is 75% less than the time required for Reference mesh, while the implementation on Mesh II reduces this computational cost to 80.2%. As a result, Mesh III is considered to be suited for obtaining numerical results free of grid effects. Therefore, the remaining results presented herein are based on Mesh III.

Figure 15 displays the snapshots of numerical solutions computed using three-level adaptive enrichments, its corresponding gradients, and adaptive quadrature points at times  $t = 30 \text{ min}$ ,  $t = 2 \text{ hours}$ ,  $t = 10 \text{ hours}$ ,  $t = 17 \text{ hours}$ , and  $t = 24 \text{ hours}$ . Notice that we use three different colors to illustrate the distributions of quadrature points namely, green color is used for the first level, blue color for the second level and red color for the third level, whereas gray color is used for those elements with smooth solutions and low concentration gradients. At the earlier time of simulations, the concentration plume released in the sea starts to develop and it is transported later on by the flow at far north around the port. The interaction between the phosphogypsum dispersion and the water flow is detected across the Jorf Lasfar zone during the simulation time. It can be clearly seen that the complicated concentration patterns are captured by the adaptive enriched semi-Lagrangian finite element method. In particular, high gradients of the concentration are well represented, as the quadrature points are condensed in regions controlled

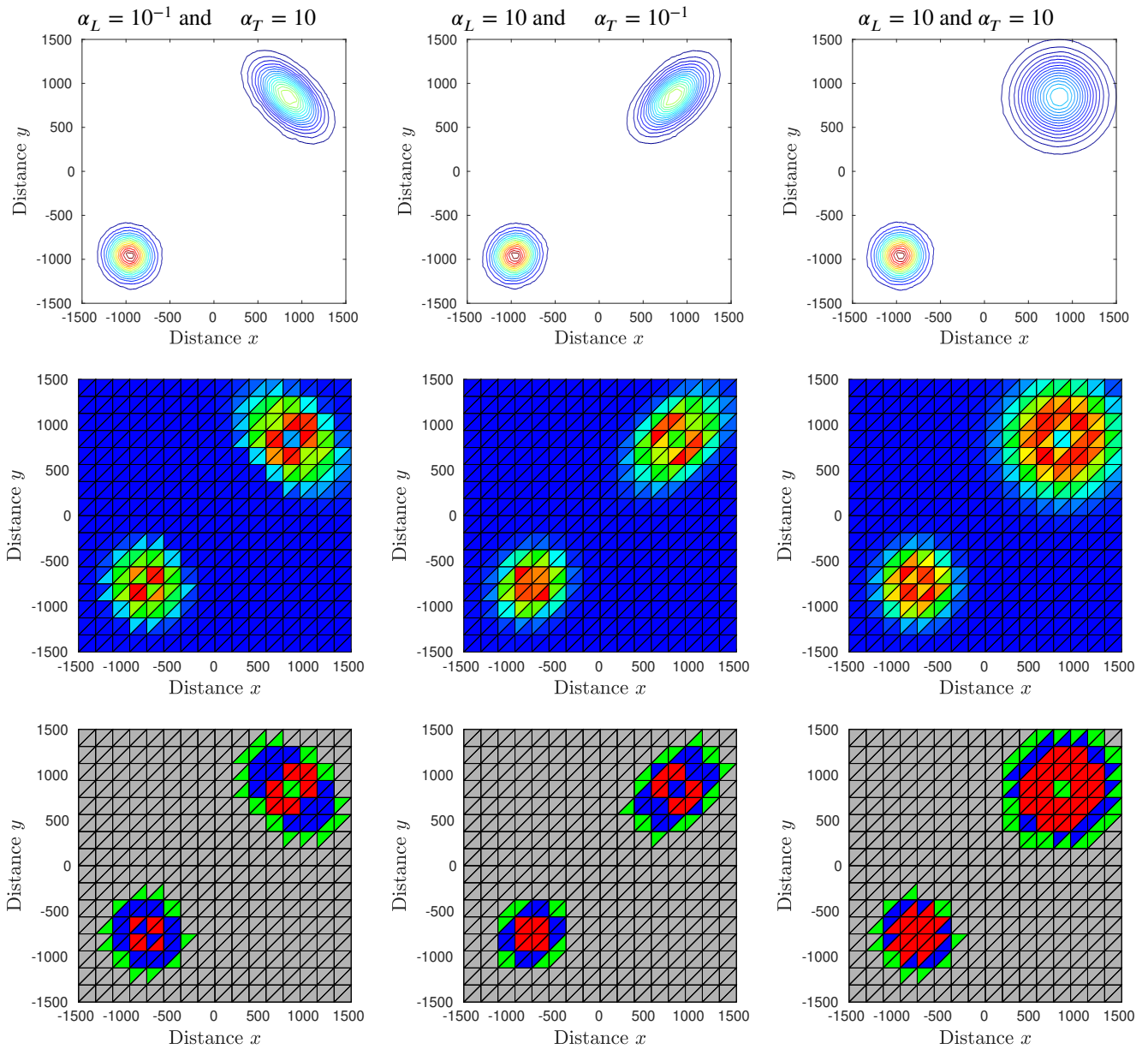


**Figure 11** Contourlines of the solution obtained by three-level adaptive enrichments (first row), gradient of the solution (second row) and adaptive quadrature points using three-level enrichments (third row) at two different times  $t = 0.4$  and  $t = 4.24$  using  $(\alpha_L = 10^{-1}, \alpha_T = 10)$  (first column),  $(\alpha_L = 10, \alpha_T = 10^{-1})$  (second column) and  $(\alpha_L = 10, \alpha_T = 10)$  (third column). For a better visualization, green, blue and red colors are used for elements with single-level, two-level, and three-level enrichments, respectively.

by the defined tolerances according to the required three-level enrichments in the computational domain. As expected, denser quadrature points are generated for the three-level adaptive enrichment than for the single- and two-level enrichments for the selected times. It can also clearly be seen from Figure 15 that, under the considered flow conditions and simulation parameters, the dispersion of phosphogypsum is mainly transported towards the same direction as suggested by the remote sensing product shown in Figure 12. For obtained flow patterns, we display in Figure 16 snapshots of the pressure and velocity magnitude along with the velocity field at time  $t = 24$  hours. The recirculation zone can be clearly seen in these results and an almost uniform pressure distribution can also be observed. Again the proposed three-level adaptive enrichment procedure captures well the pressure and velocity features in the Jorf Lasfar zone.



**Figure 12** Satellite image retrieved using Sentinel-2 product over the Jorf Lasfar region in August 2022. Dispersion of Phosphogypsum is also shown in the region bounded by the red contourline on the map.

**Table 3** Mesh statistics, values of the kinetic energy and the total averaged concentration using adaptive enrichment method at time  $t = 24$  hours, and computational times for the considered meshes in the problem of transport and dispersion of phosphogypsum in the Jorf Lasfar. The CPU times are given in seconds.

	# ele	# $P_2$ nodes	# $P_1$ nodes	Energy	Averg C	CPU
Mesh I	1849	3988	1070	2.82866	8.62122	128
Mesh II	5640	11647	3004	3.68261	11.39013	194
Mesh III	16759	34009	8659	3.73390	11.53249	245
Reference	33286	67317	17016	3.77149	11.80986	982

For comparison reasons, Figure 17 depicts the time evolution of monitored pressures, velocity magnitudes and concentrations at the three gauges shown in Figure 13 using fixed enrichments with  $N_{k,Q} = 52$ , three-level adaptive enrichments, and the conventional approach on Mesh III. Reference solutions obtained on the fine mesh using fixed enrichments with  $N_{k,Q} = 70$  are also included in these plots. It is clear that the results obtained using the conventional semi-Lagrangian finite element method suffer from excessive numerical diffusion. On the other hand, results obtained using the fixed and adaptive enrichments exhibit minor differences. The proposed multilevel adaptive enriched semi-Lagrangian finite element approach successfully captures the flow and concentration features in the Jorf Lasfar coastal zone for the considered flow, transport, and dispersion conditions. Finally, the robustness of the proposed method is compared against the conventional technique, including fixed enrichments and reference solution. Table 4 presents results for the averaged concentration volume, computational times and total kinetic energy obtained using Mesh III at time  $t = 24$  hours. Reference solutions are also included in Table 4. Both fixed and adaptive

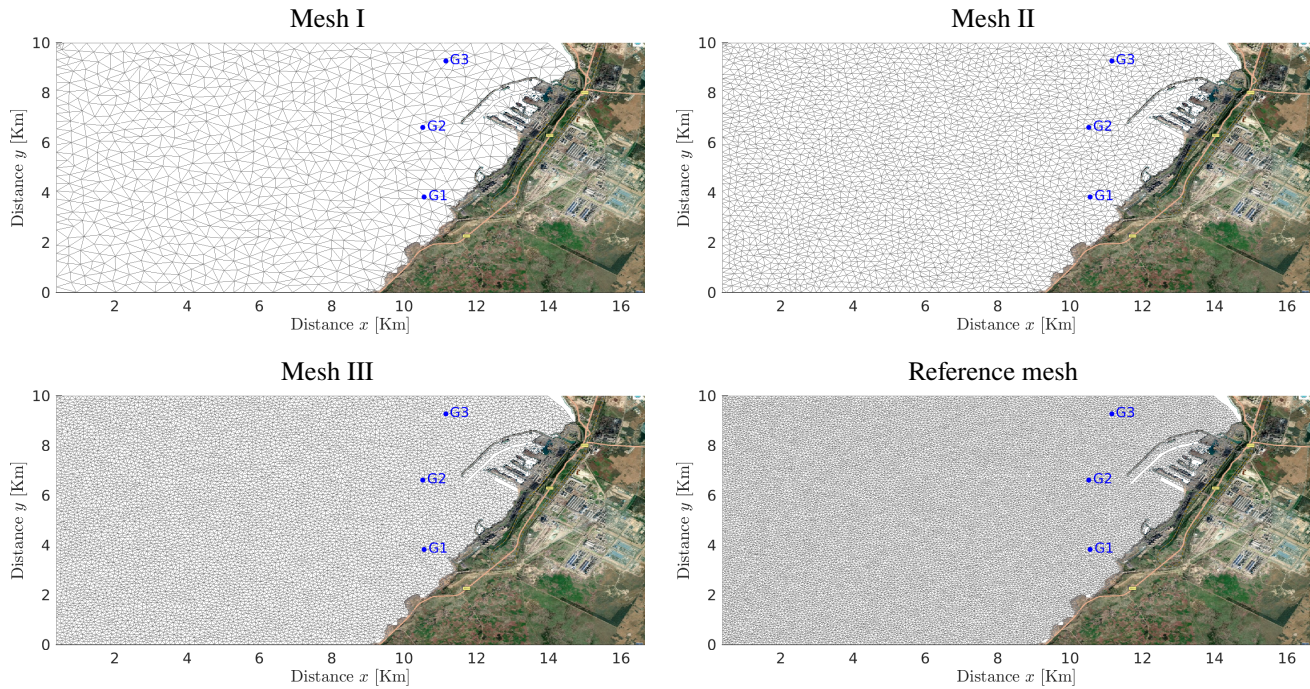


**Figure 13** Computational meshes used for the transport and dispersion of phosphogypsum in the Jorf Lasfar.

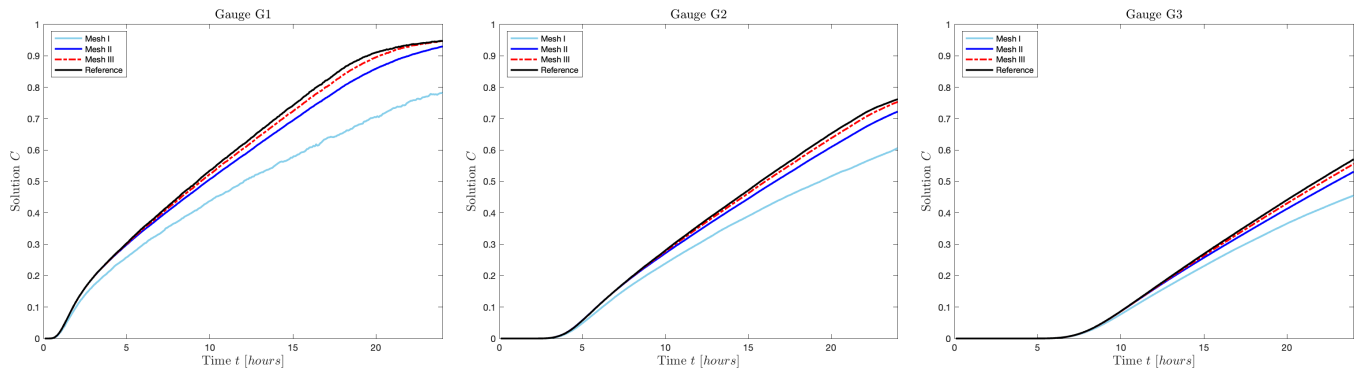


**Figure 14** Time evolution of the concentration obtained using the adaptive enrichment method at the selected gauges using different meshes for the problem of transport and dispersion of phosphogypsum in the Jorf Lasfar.

enrichments yield comparable results that are closer to reference solutions than the conventional method. In terms of CPU times, the adaptive enriched technique requires significantly less simulation time (about 63% less) than the fixed enriched method. The conventional approach has a reduced computing cost compared to the enriched approaches on the same mesh, but its overall accuracy and stability are inferior to those produced by the enrichment technique. Note that results from the proposed transport model should be compared with observations of real phosphogypsum distributions on the sea-surface in the Jorf Lasfar. However, there is no such data available until now in the literature to carry out this work. Thus, at the moment we can only perform simulations and verify that results are plausible and consistent. In summary, the phosphogypsum transport is captured accurately and the concentration front is resolved reasonably. It should be stressed that all these excellent computational features are achieved using time steps larger than those required for the Eulerian-based methods in convection-dominated flows.

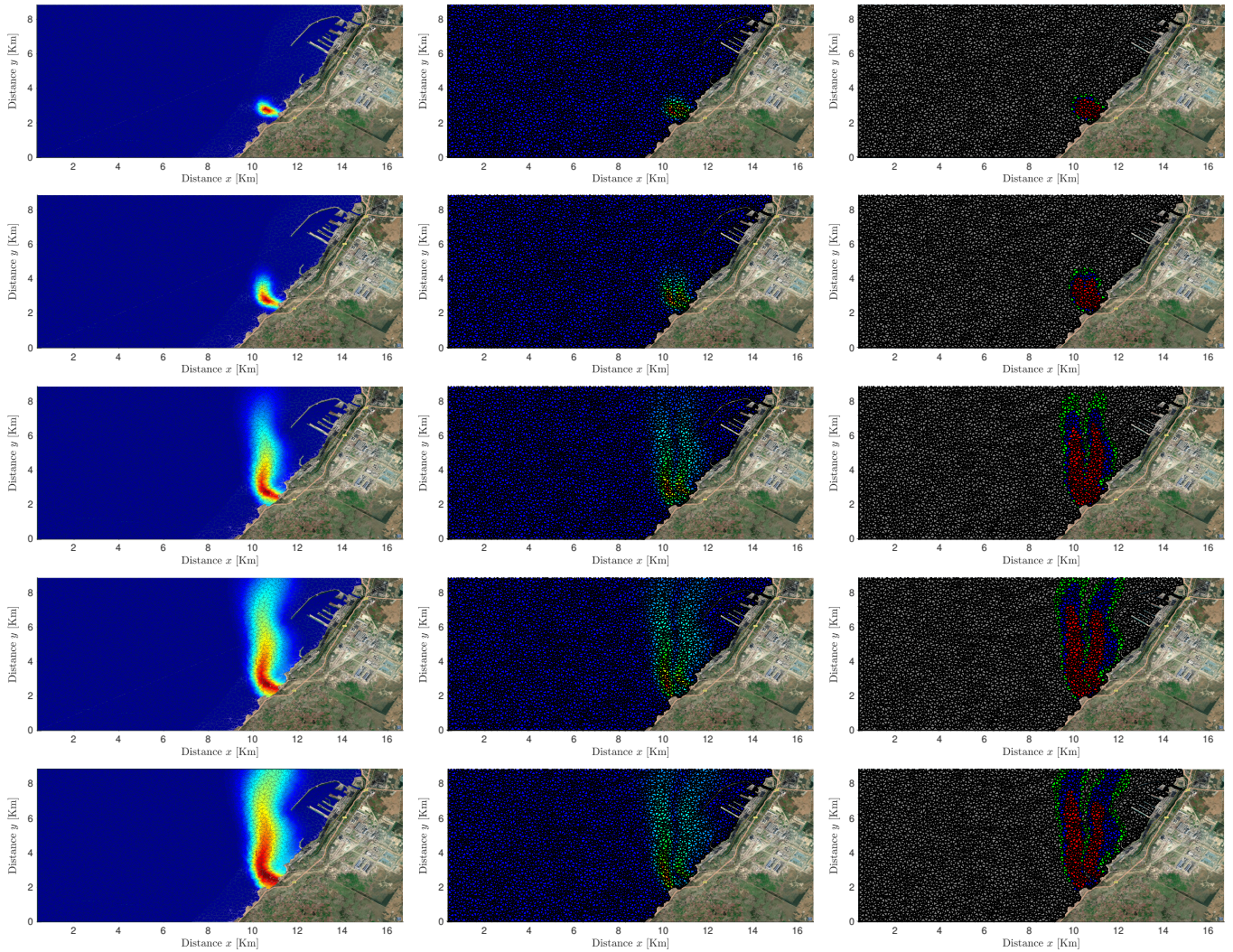


**Figure 15** Snapshots of the computed solutions on Mesh III using three-level adaptive enrichments (first column), gradient of the solution (second column) and adaptive quadrature points using three-level enrichments (third column) at time  $t = 30 \text{ min}$  (first row),  $t = 2 \text{ hours}$  (second row),  $t = 10 \text{ hours}$  (third row),  $t = 17 \text{ hours}$  (fourth row) and  $t = 24 \text{ hours}$  (fifth row). For a better visualization, green, blue and red colors are used for elements with single-level, two-level and three-level enrichments, respectively.

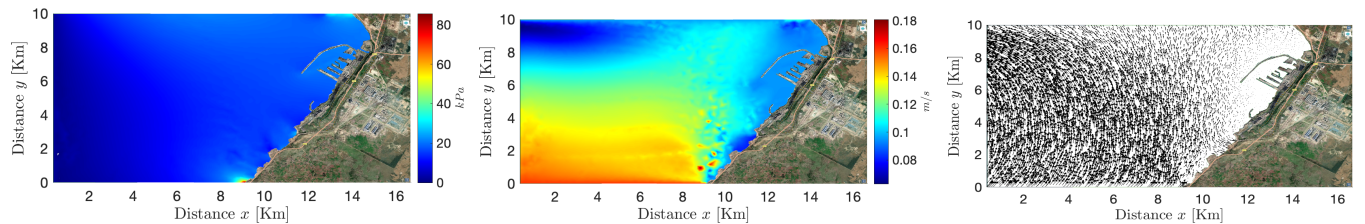


**Figure 16** Snapshot of the pressure (left), the velocity magnitude (middle) and the velocity field (right) obtained on Mesh III using three-level adaptive enrichments at time  $t = 24 \text{ hours}$ .

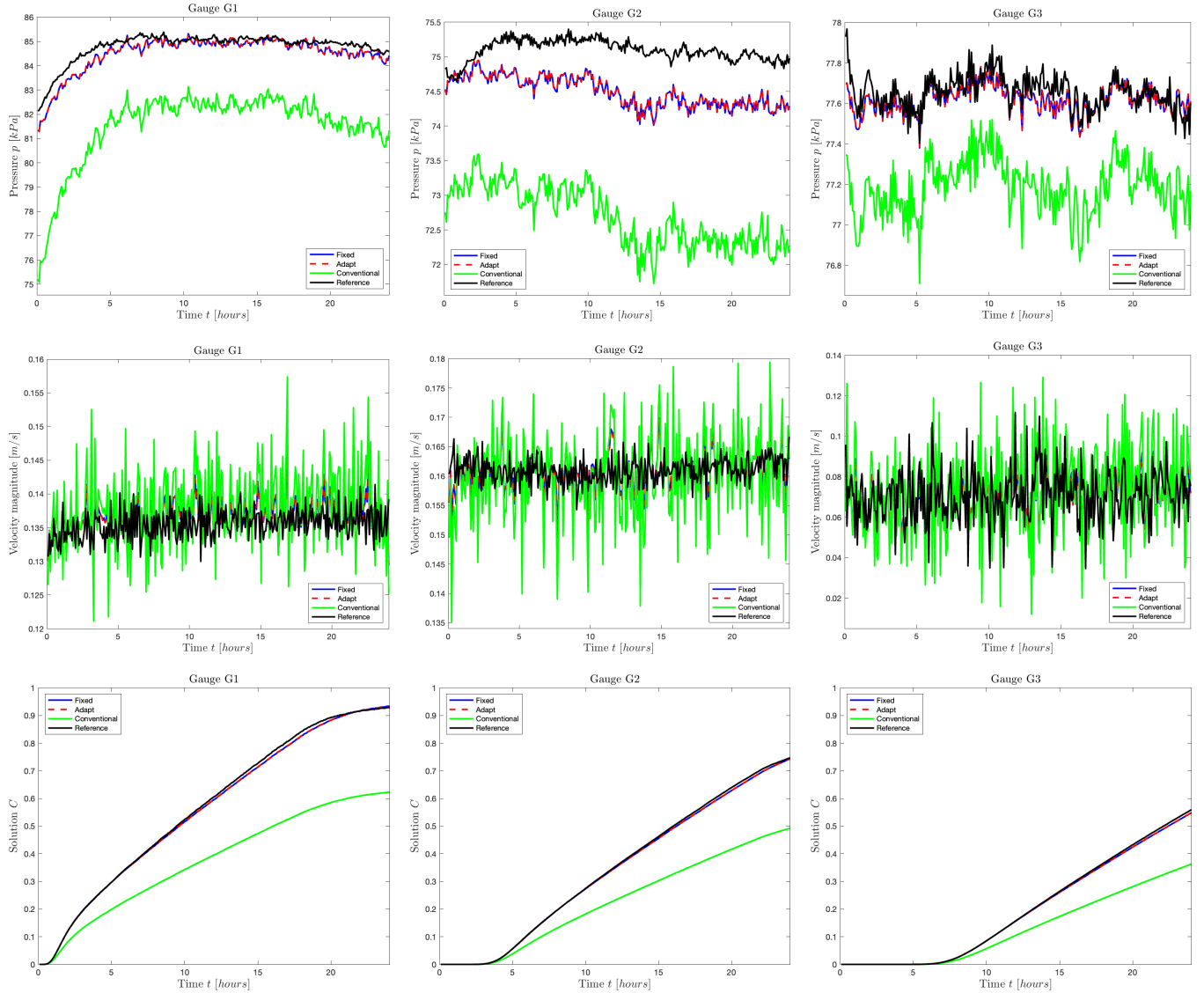


**Figure 17** Time evolution of the pressure (first row), the velocity magnitude (second row) and concentration (third row) obtained using Mesh III at the three selected gauges for the problem of transport and dispersion of phosphogypsum in the Jorf Lasfar.

## 6 | CONCLUDING REMARKS

A multilevel adaptive semi-Lagrangian finite element method is proposed in this work for modelling and simulation of transport and dispersion of phosphogypsum in the Jorf Lasfar coastal zone. To improve the efficiency and accuracy of the method, we combine the modified method of characteristics to deal with convection terms, finite element discretization to handle complex geometries, a rotational pressure-correction algorithm to solve the Stokes problem, and an adaptive  $L^2$ -projection using quadrature rules. As a result, the considered method benefits from the advantages of all these techniques to provide a semi-Lagrangian solution for dispersion problems that is efficient and accurate as well. Multilevel adaptive enrichments, in which the quadrature points are adjusted as needed without refining the mesh throughout the time integration process, have improved the accuracy and efficiency of the numerical solution. As a consequence, linear systems generated using the considered semi-Lagrangian finite element method retain the same size and structure during the adaptation process. The gradient of concentration is employed as an error indicator for adaptation of enrichments by increasing the number of quadrature points where necessary without refining the mesh. Unlike previous adaptive finite element approaches for incompressible viscous flows, linear systems in the proposed

**Table 4** Comparison results for the kinetic energy, the total averaged concentration obtained using Mesh III at time  $t = 24$  hours, and computational times for the problem of transport and dispersion of phosphogypsum in the Jorf Lasfar. The CPU times are given in seconds.

	Energy	Averg C	CPU
Conventional	1.15274	7.52275	98
Fixed	3.73761	11.53827	664
Adaptive	3.73390	11.53249	245
Reference	3.77149	11.80986	982

enriched semi-Lagrangian finite element method retain the same structure and size during the adaptation procedure. In the considered simulations, we demonstrate that the proposed approach can recover the flow characteristics on coarse meshes and with a much lower degree of freedom than the conventional method. As a result, the computational requirements are significantly reduced while maintaining the accuracy of the solutions. The development of highly accurate error estimates, such as a posteriori error estimates, will be the focus of future work and will serve as the standard for multilevel adaptive enrichment.

## 6.1 | ACKNOWLEDGMENTS

We would like to thank the Moroccan Ministry of Higher Education, Scientific Research and Innovation and the OCP Foundation who funded this work through the APRD research program.

## 6.2 | DATA AVAILABILITY STATEMENT

The data that support the findings of this study are available from the corresponding author upon reasonable request.

## References

1. Belahbib L, Arhouni F, Boukhair A, et al. Impact of Phosphate Industry on Natural Radioactivity in Sediment, Seawater, and Coastal Marine Fauna of El Jadida Province, Morocco. *Journal of Hazardous, Toxic, and Radioactive Waste* 2021; 25(1): 04020064.
2. Parreira A, Kobayashi A, Silvestre O. Influence of Portland Cement Type on Unconfined Compressive Strength and Linear Expansion of Cement-Stabilized Phosphogypsum. *Journal of Environmental Engineering* 2003; 129(10): 956-960.
3. Saadaoui E, Ghazel N, Romdhane CB, Massoudi N. Phosphogypsum: potential uses and problems – a review. *International Journal of Environmental Studies* 2017; 74(4): 558-567.
4. Cheggour M, Langston W, Chafik A, Texier H, Idrissi H, Boumezzough A. Phosphate industry discharges and their impact on metal contamination and intertidal macrobenthos: Jorf Lasfar and Safi coastlines (Morocco). *Toxicological & Environmental Chemistry* 1999; 70(1-2): 159-179.
5. El Cadi A, Fakhil Lanjri A, Laliti A, Chouaibi N, Asskali A, Khaddor M. Caractérisation de la fraction lipidique du phosphogypse: Origine et évaluation du degré de transformation des polluants organiques (Characterization of the Lipid Fraction of Phosphogypsum: Origin and Assessment of the Degree of Transformation of Organic Pollutants). *Journal of Materials and Environmental Science* 2014; 5: 2223–2229.

6. Heymans J, Bundy A, Christensen V, et al. The Ocean Decade: A True Ecosystem Modeling Challenge. *Frontiers in Marine Science* 2020; 7: 766.
7. Ryabinin V, Barbière J, Haugan P, et al. The UN decade of ocean science for sustainable development. *Frontiers in Marine Science* 2019; 6: 470.
8. Fox-Kemper B, Menemenlis D. *Can Large Eddy Simulation Techniques Improve Mesoscale Rich Ocean Models?*: 319-337; American Geophysical Union (AGU) . 2008.
9. Pearson B, Fox-Kemper B, Bachman S, Bryan F. Evaluation of scale-aware subgrid mesoscale eddy models in a global eddy-rich model. *Ocean Modelling* 2017; 115: 42 - 58.
10. Hilt M, Auclair F, Benschila R, et al. Numerical modelling of hydraulic control, solitary waves and primary instabilities in the Strait of Gibraltar. *Ocean Modelling* 2020; 151: 101642.
11. Fox-Kemper B, Adcroft A, Böning CW, et al. Challenges and Prospects in Ocean Circulation Models. *Frontiers in Marine Science* 2019; 6: 65.
12. Tang H, Liu Y. Coupling of Navier-Stokes Equations and Their Hydrostatic Versions for Ocean Flows: A Discussion on Algorithm and Implementation. In: Springer. ; 2020: 326–333.
13. Guo G, Cheng G. Mathematical modelling and application for simulation of water pollution accidents. *Process Safety and Environmental Protection* 2019; 127: 189–196.
14. Kärnä T, Kramer S, Mitchell L, Ham D, Piggott M, Baptista A. Thetis coastal ocean model: discontinuous Galerkin discretization for the three-dimensional hydrostatic equations. *Geoscientific Model Development* 2018; 11(11): 4359–4382.
15. El-Amrani M, Seaid M. A finite element modified method of characteristics for convective heat transport. *Numerical Methods for Partial Differential Equations* 2008; 24(3): 776–798.
16. El-Amrani M, Seaid M. Convergence and stability of finite element modified method of characteristics for the incompressible Navier-Stokes equations. *Journal of Numerical Mathematics* 2007; 15(2): 101–135.
17. Ouardghi A, El-Amrani M, Seaid M. An enriched Galerkin-characteristics finite element method for convection-dominated and transport problems. *Applied Numerical Mathematics* 2021; 167: 119-142.
18. El-Amrani M, Ouardghi A, Seaid M. Enriched Galerkin-Characteristics Finite Element Method for Incompressible Navier-Stokes Equations. *SIAM Journal on Scientific Computing* 2021; 43(2): A1336-A1361.
19. Ouardghi A, El-Amrani M, Seaid M. An adaptive enriched semi-Lagrangian finite element method for coupled flow-transport problems. *Computers & Fluids* 2022; 240: 105474.
20. Tanaka N, Kitayama T. Symplectic Semi-Lagrangian Schemes for Computational Fluid Dynamics. *International Journal of Computational Fluid Dynamics* 2004; 18(4): 303-308.
21. Boscheri W. A space-time semi-Lagrangian advection scheme on staggered Voronoi meshes applied to free surface flows. *Computers & Fluids* 2020; 202: 104503.
22. El Haddad M, Belhamadia Y, Deteix J, Yakoubi D. A projection scheme for phase change problems with convection. *Computers & Mathematics with Applications* 2022; 108: 109-122.
23. Popinet S. Gerris: a tree-based adaptive solver for the incompressible Euler equations in complex geometries. *Journal of Computational Physics* 2003; 190(2): 572–600.
24. Min C, Gibou F. A second order accurate projection method for the incompressible Navier-Stokes equations on non-graded adaptive grids. *Journal of Computational Physics* 2006; 219(2): 912–929.
25. Patro S, Selvam R, Bosch H. Adaptive  $h$ -finite element modeling of wind flow around bridges. *Engineering Structures* 2013; 48: 569–577.

26. Ahrabi B, Anderson W, Newman III J. An adjoint-based  $hp$ -adaptive stabilized finite-element method with shock capturing for turbulent flows. *Computer Methods in Applied Mechanics and Engineering* 2017; 318: 1030–1065.
27. De Sampaio P, Lyra P, Morgan K, Weatherill N. Petrov-Galerkin solutions of the incompressible Navier-Stokes equations in primitive variables with adaptive remeshing. *Computer Methods in Applied Mechanics and Engineering* 1993; 106(1-2): 143–178.
28. Selim K, Logg A, Larson MG. An adaptive finite element splitting method for the incompressible Navier-Stokes equations. *Computer Methods in Applied Mechanics and Engineering* 2012; 209: 54–65.
29. Wang F, Ling M, Han W, Jing F. Adaptive discontinuous Galerkin methods for solving an incompressible Stokes flow problem with slip boundary condition of frictional type. *Journal of Computational and Applied Mathematics* 2020; 371: 112700.
30. Kantha LH, Clayson CA. *Numerical models of oceans and oceanic processes*. Elsevier . 2000.
31. Kowalik Z, Murty TS. *Numerical modeling of ocean dynamics*. 5. World Scientific . 1993.
32. Lim CC, Ding X, Nebus J. *Barotropic and Shallow-Water Models in Vortex dynamics, statistical mechanics, and planetary atmospheres*. World Scientific . 2009.
33. El-Amrani M, Seaid M. A finite element semi-Lagrangian method with  $L^2$  interpolation. *International Journal for Numerical Methods in Engineering* 2012; 90(12): 1485–1507.
34. El-Amrani M, Seaid M. Numerical simulation of natural and mixed convection flows by Galerkin-characteristic method. *International Journal for Numerical Methods in Fluids* 2007; 53(12): 1819–1845.
35. El-Amrani M, Seaid M. An  $L^2$ -Projection for the Galerkin-Characteristic Solution of Incompressible Flows. *SIAM Journal on Scientific Computing* 2011; 33(6): 3110–3131.
36. Dunavant D. High degree efficient symmetrical Gaussian quadrature rules for the triangle. *International Journal for Numerical Methods in Engineering* 1985; 21(6): 1129–1148.
37. El Moçayd N, Seaid M. Data-driven polynomial chaos expansions for characterization of complex fluid rheology: Case study of phosphate slurry. *Reliability Engineering & System Safety* 2021; 216: 107923.
38. Pahlevan N, Chittimalli SK, Balasubramanian SV, Vellucci V. Sentinel-2/Landsat-8 product consistency and implications for monitoring aquatic systems. *Remote sensing of Environment* 2019; 220: 19–29.
39. Stramma L, Steele J, Thorpe S, Turekian K. Current systems in the Atlantic Ocean. *Ocean Currents* 2001: 3–12.





**Citation on deposit:** Ouardghi, A., Seaid, M., El-Amrani, M., & El Mocayd, N. (2023). A fast and accurate method for transport and dispersion of phosphogypsum in coastal zones: Application to Jorf Lasfar. *International Journal for Numerical Methods in Fluids*, <https://doi.org/10.1002/fld.5248>

**For final citation and metadata, visit Durham Research Online URL:**  
<https://durham-repository.worktribe.com/output/1930983>

**Copyright statement:** This accepted manuscript is licensed under the Creative Commons Attribution 4.0 licence.

<https://creativecommons.org/licenses/by/4.0/>